

Modified deformation behaviour of self-ion irradiated tungsten: A combined nano-indentation, HR-EBSD and crystal plasticity study

Suchandrima Das^{a*}, Hongbing Yu^a, Kenichiro Mizohata^b, Edmund Tarleton^{a,c}, Felix Hofmann^{a†}

^a*Department of Engineering Science, University of Oxford, Parks Road, Oxford OX1 3PJ, UK*

^b*Accelerator Laboratory, University of Helsinki, P.O. Box 64, 00560 Helsinki, Finland*

^c*Department of Materials, University of Oxford, Parks Road, Oxford OX1 3PH, UK*

**suchandrima.das@eng.ox.ac.uk*

†*felix.hofmann@eng.ox.ac.uk*

Keywords

crystal plasticity; polycrystalline material; electron microscopy; non-destructive evaluation; mechanical testing

Abstract

Predicting the dramatic changes in mechanical and physical properties caused by irradiation damage is key for the design of future nuclear fission and fusion reactors. Self-ion irradiation provides an attractive tool for mimicking the effects of neutron irradiation. However, the damaged layer of self-ion implanted samples is only a few microns thick, making it difficult to estimate macroscopic properties. Here we address this challenge using a combination of experimental and modelling techniques. We concentrate on self-ion-implanted tungsten, the front-runner for fusion reactor armour components and a prototypical bcc material. To capture dose-dependent evolution of properties, we experimentally characterise samples with damage levels from 0.01 to 1 dpa. Spherical nano-indentation of $\langle 001 \rangle$ grains shows hardness increasing up to a dose of 0.032 dpa, beyond which it saturates. AFM measurements show pile-up increasing up to the same dose, beyond which large pile-up and slip-steps are seen. Based on these observations we develop a simple crystal plasticity finite element (CPFE) model for the irradiated material. It captures irradiation-induced hardening followed by strain-softening through the interaction of irradiation-induced-defects and gliding dislocations. The shear resistance of irradiation-induced-defects is physically-based, estimated from TEM observations of similarly irradiated samples. Nano-indentation of pristine tungsten and implanted tungsten of doses 0.01, 0.1, 0.32 and 1 dpa is simulated. Only two model parameters are fitted to the experimental results of the 0.01 dpa sample and are kept unchanged for all other doses. The peak indentation load, indent surface profiles and damage saturation predicted by the CPFE model closely match our experimental observations. Predicted lattice distortions and dislocation distributions around indents agree well with corresponding measurements from HR-EBSD. Finally, the

CPFE model is used to predict the macroscopic stress-strain response of similarly irradiated bulk tungsten material. This macroscopic information is the key input required for design of fusion armour components.

1. Introduction

The lifetime of plasma-facing armour components in future fusion reactors will be compromised due to in-service irradiation by fusion neutrons and gaseous elements such as hydrogen and helium (Entler et al., 2018; Knaster et al., 2016). Irradiation induces significant changes in the physical and mechanical properties, such as increased hardening, embrittlement, dimensional change, residual stress, reduced thermal conductivity etc. (Armstrong et al., 2013; S. Das et al., 2018a, 2018b; Fang et al., 2018; Hofmann et al., 2015a; Yi et al., 2013). Making armour components more resistant to radiation and accurate prediction of their lifetime will be essential for realising commercial fusion power. This requires fundamental study of the change inducing factors; nucleation and evolution of irradiation-induced defects, and their interaction for example with glide dislocations. Since fusion reactor conditions cannot be recreated yet, such studies are commonly done using representative models of inactive, ion-implanted metals. For example, helium-implanted and self-ion-implanted materials are used as representative models of helium-irradiated and neutron-irradiated materials respectively (Armstrong et al., 2011; DeBroglie et al., 2015; Gibson et al., 2015; Heintze et al., 2011).

Ion-implantation is inexpensive and allows isolated investigation of displacement damage effects up to high dose levels (a few hundred displacements per atom (dpa)), without the added complexity of transmutation and gas evolution (Dennett et al., 2018; Toloczko et al., 2014). However, the ion-implanted damage layer is only a few microns thick (precise depth

depends on the ion energy used and the atomic number of the ions and target material) and thus too thin for conventional, macroscopic testing approaches. Nano-indentation is commonly used to probe the mechanical properties of these thin ion-implanted layers (Heintze et al., 2009; Hosemann et al., 2009; N. Li et al., 2009; Oliver and Pharr, 2004). Further characterisation of the deformation behaviour of the ion-implanted layer, can be done by examining the deformation field around and beneath indents using techniques such as high-resolution electron back-scattered diffraction (HR-EBSD) ((Wilkinson, 1996), 3D Laue diffraction (S. Das et al., 2018a), high-resolution digital image correlation (HR-DIC) (Guan et al., 2017) etc. Additionally examination of lift-out samples from the ion-implanted layer by transmission electron microscopy (TEM) can give direct information about the defect microstructure induced by implantation (Yi, 2013). Such experimental characterisation can be performed on ion-implanted samples with systematically varying crystallographic orientation, varying damage dose, varying temperature conditions or different impurity concentrations. Through these studies the influence of these different parameters on the formation and structure of irradiation-induced defects and resulting changes in material properties can be probed.

Information gathered from the combination of these characterisation techniques corresponds to the thin irradiated layer. However, for reactor design, it is essential to “translate” this information to estimate the deformation behaviour of a similarly irradiated macroscopic polycrystal. This can be done by using the small-scale response information from the thin ion-implanted layer to develop a mesoscale model of the ion-damaged material. Importantly this must capture the key physics controlling property change, accounting for example for the interaction between expected defect-types and gliding dislocations, considering orientation-dependence etc. Furthermore, model parameter should be linked to

dose-related observables such as defect density obtained from TEM. Once tuned and validated against experimental observations, this mesoscale model can then be used to predict the deformation response of a similarly irradiated macroscopic polycrystal; a task challenging to achieve experimentally owing to limited ion-penetration depth. Here we demonstrate all the parts of this process using tungsten as a prototypical material.

Tungsten is the most promising material for plasma-facing armour components in future fusion reactors (Maisonnier et al., 2005; Wei et al., 2014). Its high melting point (3422 °C), low tritium-retention rate, low sputtering rate and good thermal conductivity, make it suitable for withstanding the harsh conditions anticipated in service. However, past studies show undesirable irradiation-induced changes in its properties. In-situ TEM of tungsten implanted with 150 keV self-ions, at room temperature, showed that the first observable defects (predominantly $\frac{1}{2}\langle 111 \rangle$ vacancy loops) appear at very low doses < 0.01 dpa. Their concentration increases almost linearly with dose before saturating at higher doses (0.1 - 1 dpa) (Yi et al., 2016). Nano-indentation of tungsten-implanted tungsten layers have shown that these defects can cause significant hardening (Armstrong et al., 2013; Gibson et al., 2014), with suppression of pile-up around indents indicating a substantial strain hardening (Armstrong et al., 2011). Also, reduction in thermal diffusivity and ductility is expected to be caused by irradiation defects (Hofmann et al., 2015a; Reza et al., 2019; Zinkle and Was, 2013).

To integrate these changes into a material model, quantitative understanding of the underlying mechanisms is required. However, such understanding is difficult to derived conclusively from past studies: For example, the suppression in pile-up noticed around indents in self-ion-implanted tungsten is unexplained (Armstrong et al., 2011). This is particularly surprising, as it is in stark contrast to indents in helium-implanted tungsten which

show a large increase in pileup (alongside irradiation hardening), and slip channels indicative of strain-softening (Beck et al., 2017; S. Das et al., 2018a). This raises the question as to whether the interaction of gliding dislocations with implantation defects in tungsten-implanted tungsten is different from that in helium-implanted case and why this would be the case.

Here we aim to address these questions and develop an understanding of the physics of irradiation induced changes, by characterising self-ion-implanted tungsten samples using scanning electron microscopy (SEM), atomic force microscopy (AFM), HR-EBSD and TEM data. We consider polycrystalline tungsten samples (99.99% purity), implanted at room temperature and exposed to a range of damage levels (0.01, 0.1, 0.32 and 1 dpa). Based on our understanding from experimental results, we develop a material model representative of the self-ion implanted tungsten at varying doses. We verify the material model formulation by comparing its predictions of deformation behaviour with corresponding experimental results. Finally, we use the verified material model to predict the deformation behaviour of similarly irradiated macroscopic self-ion implanted polycrystalline tungsten.

While the outlook is to build material models accounting for all possible parameters (like temperature, purity, orientation, dose) influencing the implantation-induced changes in material properties, the effect of each parameter must first be considered individually, before incorporating into one model. Considering the complexity of the task, we start here by accounting for two parameters; crystallographic orientation and implantation dose. To avoid influences of other parameters like temperature and impurity, high purity samples implanted at room temperature are considered here.

2. Experimental Methods

2.1. Sample preparation

Seven samples, of size 1 cm square with a thickness of 1 mm were cut from a polycrystalline tungsten sheet (99.99 wt% purity, procured from Plansee) and then annealed at 1500 °C for 24 h in vacuum ($\sim 10^{-5}$ mbar). A high quality, damage free surface finish was obtained by mechanical grinding, polishing with diamond paste and colloidal silica, and finally electropolishing in an electrolyte of 1% NaOH aqueous solution (8 V, room temperature).

2.2. Ion implantation

High energy ion implantation was performed to mimic neutron-induced damage. Implantation with 20 MeV tungsten ions was used (+5 charge state, 5 MV tandem accelerator (Tikkanen et al., 2004)), to create a relatively homogeneous damage profile across a ~ 2.5 μm thick layer (Hosemann et al., 2012).

Implantations were carried out at room temperature. The ion beam was raster scanned across the sample area ($\sim 15 \times 15$ mm²) with a sweeping frequency of ~ 5 - 10 Hz in both X and Y directions, and was slightly defocused to make the spot diameter of ~ 5 mm. Beam current and dose before the target chamber were monitored using a beam profilometer (BPM). The BPM current measurement was calibrated using a faraday cup (f-cup) in the target chamber. A 12.5 mm diameter collimator was placed in front of the f-cup to define the area of the f-cup. The beam current and exposure time were adjusted to obtain the desired damage levels (Table 1). The same flux density was used for all implantations.

Figure 1 (a) shows distribution of damage and ion-ranges estimated using the SRIM code (Ziegler and Biersack, 2010) (quick Kinchin-Pease method, 68 eV displacement energy (ASTM

International, West Conshohocken, PA, 2009, 2009). The damage level listed in Table 1 refers to the peak of the damage profile.

Dose level (dpa)	Fluence (ions/cm ²)	Flux (ions/cm ² /s)
0.01	2.55×10^{12}	$3.1 - 5.0 \times 10^{10}$
0.018	4.61×10^{12}	$3.1 - 5.0 \times 10^{10}$
0.032	8.20×10^{12}	$3.1 - 5.0 \times 10^{10}$
0.1	2.54×10^{13}	$3.1 - 5.0 \times 10^{10}$
0.32	8.11×10^{13}	$3.1 - 5.0 \times 10^{10}$
1	2.53×10^{14}	$3.1 - 5.0 \times 10^{10}$

Table 1 – List of the different damage levels considered and the corresponding implantation fluence and flux used for the self-ion implanted tungsten.

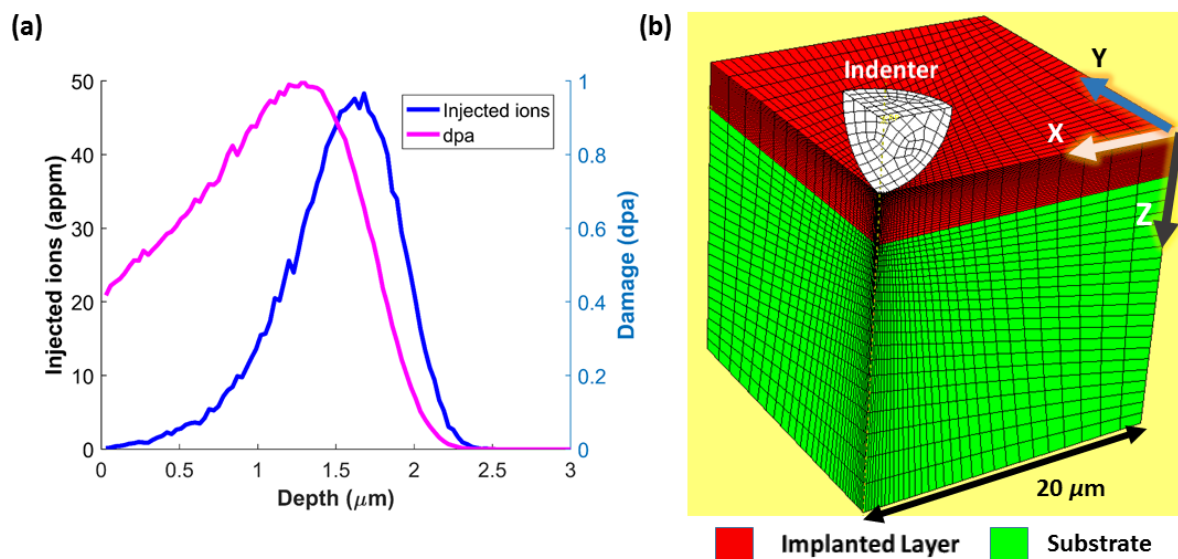


Figure 1 – (a) SRIM estimate of the injected ion concentration (blue curve) and the implantation induced displacement damage (pink curve) as a function of depth in the tungsten sample damaged to 1 dpa. The profiles for the other damage levels simply correspond to scaled versions of these profiles. (b) CPFE mesh of the quarter model created in Abaqus for simulation of the nano-indentation experiments.

2.3. Choice of test points

Electron back scatter diffraction (EBSD) was used to identify three suitable grains with near <001> surface normal orientation in each sample. In addition a <011> and a <111> oriented

grain were also identified in the unimplanted and the 1 dpa sample to investigate orientation dependence of the indentation response. The exact orientations of the chosen grains are listed in Appendix A.

2.4. Nano-indentation & Atomic force microscopy

In each of the chosen grains (Table A.1), a 500 nm deep indent was made with a spherical indenter tip of radius $\sim 5 \mu\text{m}$ (MTS NanoXp, Synton diamond tip). Grains were chosen to allow a spacing of at least $50 \mu\text{m}$ between indents.

Atomic force microscopy was used to measure the surface height profile in the vicinity of each indent. These measurements were done in contact mode using a Digital Instruments Dimension 3100 AFM with Bruker CONTV-A tips (10 nm nominal tip radius).

2.5. HR-EBSD

Residual elastic lattice strain and lattice rotation tensors were experimentally measured using the high angular resolution EBSD (HR-EBSD) technique (Wilkinson et al., 2006). A Kikuchi diffraction pattern was collected for each point at a resolution of 600×800 pixels using a conventional EBSD setup. EBSD experiments were performed in a Zeiss Merlin field emission gun SEM. Accelerating voltage of 20 keV and beam current of 15 nA was chosen. A Bruker e-flash high definition EBSD detector was used to collect EBSD patterns. The EBSD maps were acquired using 169 nm step size. The maps were analysed using the XEBSD code (provided by A. J. Wilkinson (Wilkinson et al., 2006)) to probe the distortion of diffraction patterns with respect to a reference pattern chosen from a nominally strain free region within the same grain. The measured distortions can be linked to the elastic deformation gradient, \mathbf{F}^e , i.e. the elastic component of the two-point tensor, that maps the undeformed state to the deformed state (Suchandrima Das et al., 2018a). From \mathbf{F}^e , the elastic strain ($\boldsymbol{\varepsilon}^e$) and rotation ($\boldsymbol{\omega}^e$) are determined. To ensure reliable measurements, correlation with 40 regions of interest was

used. Since a lattice dilatation will not cause a distortion of the Kikuchi pattern, the lattice strain, ϵ^e , measured by HR-EBSD only contains deviatoric components. Further details about the HR-EBSD technique can be found elsewhere (Britton and Hickey, 2018; Pantleon, 2008; Wilkinson, 1996; Wilkinson et al., 2006).

3. Experiments to guide CPFEE formulation

Initial experiments were conducted on grains of three different orientations in the unimplanted and the 1 dpa samples, to develop a hypothesis for the underlying defect-dislocation interaction on which the crystal plasticity formulation might be based. These two extremes were chosen as they should most prominently show the differences brought about by self-ion implantation.

Figure 2(a) shows AFM micrographs of indents in $\langle 001 \rangle$, $\langle 011 \rangle$ and $\langle 111 \rangle$ grains in the unimplanted and 1 dpa sample. While little difference is seen between indents in the unimplanted sample, a clear orientation dependence is observed in the 1 dpa sample. The $\langle 001 \rangle$ oriented grain shows substantial pile-up, while the other two orientations show little pile-up. This observation has two important implications:

First it may explain the seemingly contradictory indent surface morphologies reported in different self-ion implanted materials. Indents in self-ion implanted W-5wt%Ta showed suppression of pile-up (Armstrong et al., 2011), while a pile-up increase was seen around indents in self-ion implanted Fe-12wt% Cr (Hardie et al., 2015). Neither study mentions the crystallographic orientation of the grain under investigation. As such it is quite possible that the reported marked differences are simply the result of different grain orientations being

probed (e.g. near $\langle 001 \rangle$ orientation in Fe-12 wt%Cr (Hardie et al., 2015) and a near $\langle 011 \rangle$, $\langle 111 \rangle$ or an in-between orientation in W-5wt% Ta (Armstrong et al., 2011)).

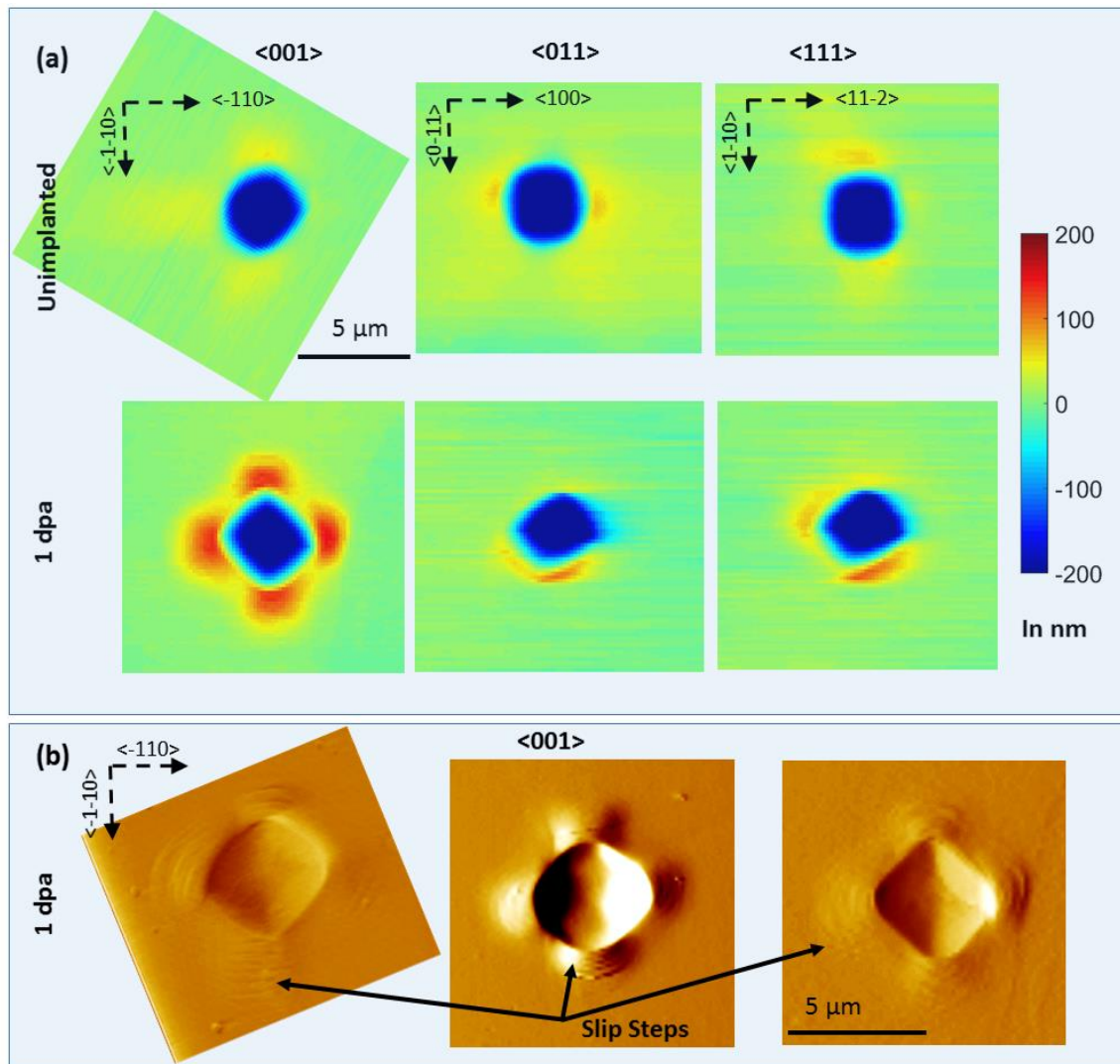


Figure 2 – (a) AFM micrographs of 500 nm deep indents in grains of three different orientations ($\langle 001 \rangle$, $\langle 011 \rangle$ and $\langle 111 \rangle$) in the unimplanted and 1 dpa self-ion implanted tungsten samples. For each orientation, the micrographs in both samples, have been rotated to maintain the same in-plane orientations. (b) Magnified view of AFM gradient images of indents in three $\langle 001 \rangle$ grains in the 1 dpa sample clearly showing the formation of slip steps.

The second key implication is derived from the surprising likeness between the orientation-dependent pile-up patterns noticed here and those observed in 3000 appm

helium implanted tungsten (W-3000He)¹ (Das et al., 2019). In particular, the localisation of pile-up and slip steps around the <001> indents in the 1 dpa sample (Figure 2b) closely match the observations from indents in <001>-oriented grains of W-3000He.

In W-3000He, the mechanism of deformation in the presence of implantation defects, was found to be orientation-independent, and a physically-based CPFEE formulation, implementing strain-softening, could reproduce the varying pile-up pattern for all orientations (Das et al., 2019). The formulation was based on observations from several different experimental studies, as well as multi-scale simulations. Ab-initio calculations and lattice strain measurements suggest a damage microstructure dominated by helium-filled Frenkel-pairs [(Becquart and Domain, 2009; Hofmann et al., 2015b)]. Based on the observations of increased hardening, slip traces near indents (observed by SEM) and reduced defect density channels beneath indents (observed by TEM), it was hypothesized that helium-filled Frenkel defects initially act as effective obstacles to glide dislocations. However, their obstacle strength is reduced by the passage of dislocations (probably due to glide-dislocation-assisted recombination of some of the Frenkel defects), leading to a localisation of deformation in slip channels (Suchandrima Das et al., 2018b).

Considering the remarkable similarity in observations from nano-indentation of self-ion- and helium- implanted tungsten (large pile-up and slip traces around <001> indents, reduced pile-up around <011> and <111> indents and increased hardening (Armstrong et al., 2013; Das et al., 2019)), we propose that although the defect microstructure induced by the two implantation conditions is distinctly different, orientation-independent strain-softening

¹ In helium-implanted tungsten too, a large pile-up was seen for indents in <001> grain orientation and very little pile-up for indents in the <011> and <111> grain orientations.

occurs during deformation in both cases. We hypothesize that in self-ion implanted materials too, the defect-dislocation interaction mechanism is orientation-independent. Rather differences in surface morphology arise simply as a result of the relative orientation between the crystal, the sample surface and the spherical nano-indenter (Das et al., 2019).

Thus a modified version of the CPFEE formulation used to model W-3000He is developed for self-ion implanted tungsten. The important difference is that, instead of considering the interaction of glide dislocations with helium-filled Frenkel pairs, we explicitly account for the interaction of glide dislocations with irradiation-induced dislocation loops. Information about the density and size distribution of the dislocation loops at varying doses is obtained from TEM and directly linked to the model parameters. Simulations of the nano-indentation process are performed for a number of different self-ion damage levels, concentrating on grains with $\langle 001 \rangle$ orientation, where pile-up is expected to be highest. To examine the accuracy of the formulation, its predictions at varying dose levels, are directly compared to AFM and HR-EBSD measurements.

4. CPFEE Formulation

The nano-indentation experiments were simulated using a strain-gradient crystal plasticity model where dislocation slip was restricted to occur in slip directions compatible with the crystallography. The finite element software Abaqus 2016 (Dassault Systèmes, Providence, RI, USA), was used to simulate the indentation model. The crystal plasticity model was implemented in an Abaqus user material subroutine (UMAT). The model was constructed as having $\langle 001 \rangle$ crystallographic orientation, similar to the physical sample.

4.1. The CPFEE Model

A 3D model comprising of a $20 \times 20 \times 20 \mu\text{m}^3$ deformable block and a rigid $5 \mu\text{m}$ radius spherical indenter was constructed (Figure 1(b)). Considering symmetry for the $\langle 001 \rangle$ grain

orientation, only a quarter of the experimental setup was modelled. Symmetry boundary conditions were applied on the XZ and YZ planes. The top surface was traction free and all other surfaces were fixed. The 20 μm high sample block was partitioned into two layers: a 2.5 μm thick implanted surface layer and a 17 μm thick substrate (Figure 1 (b)). The indenter was considered a discrete rigid wire frame while the sample block was modelled with isotropic elastic properties for tungsten (values in Appendix C). A frictionless hard contact was assumed between the indenter and the sample surface, as the mechanical response has been found to be insensitive to friction co-efficient (Wang et al., 2004). As in the experiments, displacement-controlled loading was simulated where the indenter was subjected to a displacement of 0.5 μm into the sample block before unloading. The simulated load was scaled with an effective modulus E_{eff} to account for the indenter tip compliance (Appendix B). The sample block was meshed using 20-node 3D quadratic hexahedral elements, with reduced integration (8 integration points) (C3D20R). A refined mesh (applied edge bias 0.1 to 2 μm) with 39500 elements was used (Figure 1 (b)).

4.2. UMAT formulation for pure tungsten

The user element (UEL) originally developed by Dunne et al. (Dunne et al., 2007) forms the basis of the CPFE implementation. A detailed description can be found elsewhere (Suchandrima Das et al., 2018a; Dunne et al., 2007). Briefly, the slip law used is physically-based and considers the thermally activated glide of dislocations in a field of pinning dislocations. When the yield criterion is satisfied i.e. the resolved shear stress on slip system λ , τ^λ , is greater than the critically resolved shear stress (CRSS), τ_c , the crystallographic slip rate $\dot{\beta}_p^\lambda$ for slip system λ is given by

$$\dot{\beta}_p^\lambda(\tau^\lambda) = \rho_m b^2 v \exp\left(-\frac{\Delta F}{kT}\right) \sinh\left(\frac{(|\tau^\lambda| - \tau_c)V}{kT}\right) \text{sgn}(\tau^\lambda) \quad (1)$$

where, ρ_m , is the density of mobile dislocations, ν the attempt frequency, b , the Burgers vector magnitude, ΔF , the activation energy, k the Boltzmann constant, T the absolute temperature, and V the activation volume, which depends on the spacing between the pinning dislocations, l . l is estimated as $\frac{1}{\sqrt{\Psi(\rho_{SSD})}}$, where, coefficient Ψ represents the probability of pinning by ρ_{SSD} i.e. the density of statistically stored dislocations (SSD). The values of the material parameters used here are provided in Appendix C. Assumptions of isotropic elasticity and small elastic deformations were made in the formulation. Also, for simplicity, all parameters on the RHS in Eq. (1) were kept unchanged, other than τ_c (considered the same for all slip-systems) and the independent variable τ^λ .

The critically resolved shear stress (CRSS) at any point in the material is

$$\tau_c = \tau_c^0 + C' G b \sqrt{\rho_{GND}}. \quad (2)$$

The first term on the RHS of (2), τ_c^0 , is the CRSS of the pure unimplanted tungsten. As the material deforms plastically, new dislocations are created to accommodate the lattice curvature, i.e. geometrically necessary dislocations (GNDs) (Suchandrima Das et al., 2018a; Nye, 1953). The evolution of these GNDs increases the number of obstacles encountered by gliding dislocations. The second term accounts for this strain hardening using a Taylor hardening law (Davoudi and Vlassak, 2018; Taylor, 1934) where C' is a hardening factor, G the shear modulus of tungsten and ρ_{GND} the sum of the GNDs produced across all slip-systems. Only two parameters were fitted to the experimental results (nano-indentation and AFM surface profile) of the unimplanted sample; τ_c^0 , and C' .

For simulating indentation of pristine tungsten, both layers of the model were assigned the properties of the unimplanted material. When simulating indentation of the self-ion implanted tungsten sample, material parameters for the undamaged substrate layer were

kept unaltered, while additional features were added to the top layer representing the self-ion implanted tungsten (Section 4.3).

4.3.UMAT formulation of self-ion implanted tungsten

Based on the observations from the 1 dpa implanted sample (Section 3), the UMAT formulation for self-ion implanted tungsten is built on the same strain-softening formulation as used for helium-implanted tungsten (Suchandrima Das et al., 2018b). The hypothesis is that initially the self-ion induced loops pose strong obstacles to gliding dislocations, causing hardening. However, their strength is reduced by glide dislocations cutting through them (details in Section 4.3.1). This leads to the localisation of deformation in channels and hence the formation of slip steps.

To implement this hypothesis, Eq. (2) is modified for the implanted layer by including an extra term accounting for the additional shear resistance τ_H (with initial value τ_H^0 at $t = 0$) of the implantation-defects

$$\tau_c = \tau_c^0 + C' G b \sqrt{\rho_{GND}} + \tau_H. \quad (3)$$

To implement strain-softening, i.e. the progressive weakening of defects by gliding dislocations, τ_H is reduced at the end of each time increment Δt , as a function of the accumulated crystallographic slip, β_p :

$$\beta_p^{t+\Delta t} = \beta_p^t + \sum_{\lambda=1}^n \dot{\beta}_p^\lambda \Delta t \quad (4)$$

$$\tau_H^{t+\Delta t} = \tau_H^0 e^{-(\beta_p^{t+\Delta t}/\gamma)} \quad (5)$$

where, β_p^t and $\beta_p^{t+\Delta t}$ are the accumulated slip summed over all slip systems at the start and end of increment Δt . The rate of defect removal is likely to be proportional to its current value

i.e. the current defect concentration² (Suchandrima Das et al., 2018b) resulting in the exponential softening rate in Eq. (5).

Thus two new parameters are introduced in the implanted layer; τ_H^0 and the softening rate γ (Eq. (5)). Of these, only γ is fitted to the experimental data of the 0.01 dpa implanted sample and is kept constant in simulations for all other damage levels. τ_H^0 is physically-based and derived from TEM data of defect density for the different damage levels as described in Section 4.3.1

4.3.1. Determining τ_H^0

τ_H^0 , the initial value of the implantation-induced shear resistance force, is computed specifically for each damage level based on the implantation-induced loop number density determined by TEM as a function of damage (Yi et al., 2016). In doing so the implicit assumption is made that loops smaller than 1.5 nm, i.e. below the resolution limit of TEM, have little effect on dislocation glide.

Yi et al. (Yi et al., 2016) studied tungsten samples implanted with 150 keV W⁺ ions at 300 K for a range of damage levels from 0.01 up to 1 dpa. Though the ion implantation energy in the referred study is different from that used here, the data is relevant because of the comparable dpa levels.

² $\left. \frac{\partial \tau_H}{\partial \beta_p} \right|_{t+\Delta t} = -\tau_H/\gamma$

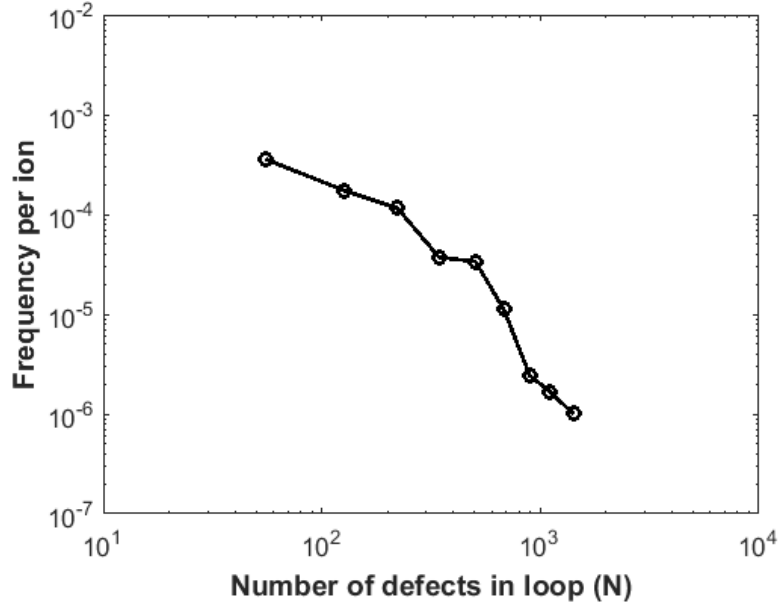


Figure 3 – Plot of data points extracted from (Yi et al., 2016) showing the frequency of occurrence (f) of a loop containing N point defects for every implanted ion for tungsten implanted with self-ions at 300 K to 0.01 dpa.

We start by considering the TEM observations for a damage level of 0.01 dpa. At this early stage of damage there is negligible cascade overlap (Yi et al., 2016)). For this case, TEM observations detailing the frequency of occurrence (f) of a loop containing N point defects per implanted ion (Figure 3 in (Yi et al., 2016)) can be determined (extracted data points in Table 2, columns 1 and 2 and plotted in (Figure 3). From the data in Figure 3, L_d^N i.e. the number density of loops (in loops/m²) of diameter d and containing N point defects within the implanted layer of the TEM foil can be calculated. The loop diameter d can be computed from N as

$$d = \sqrt{N} \frac{2a}{3^{1/4} \sqrt{\pi}} \quad (6)$$

where, a is the lattice parameter (0.31652 nm for tungsten (Derlet et al., 2007; Hofmann et al., 2015b)). Eq. (6) is derived based on the assumption that all visible defects are $\frac{1}{2}\langle 111 \rangle$ circular prismatic dislocation loops with area $A = \pi d^2/4$ containing $N = Ab/V$ atoms, with

atomic volume, $V = a^3/2$, and Burgers vector length, $b = \sqrt{3}a/2$, for bcc tungsten (Yi et al., 2016).

In Yi et al. (Yi et al., 2016) the bins in the plots are defined as $[N(d - 0.5), N(d + 0.5)]$ (d being the loop diameter in nm) and f is normalized to the bin width and the ion-fluence φ (which for 0.01 dpa is 1×10^{16} ions/m²). Thus, for a given value of N from the plot, we can use Eq. (6) to compute the corresponding loop diameter, d , and thereby the corresponding bin width, B_w , as

$$B_w = N(d + 0.5) - N(d - 0.5) \quad (7)$$

Knowing φ , we can compute the loop number density L_d^N

$$L_d^N = f\varphi B_w. \quad (8)$$

L_d^N here is the loop number density (in loops/m²) for the whole thickness of the irradiated layer in the TEM foil, which in this case is $D = 25$ nm (the total foil thickness is reported as 66 nm (Yi et al., 2016) and the irradiated layer thickness is ~ 25 nm). Here we assume that the loops are uniformly stacked with zero vertical spacing throughout the 25 nm thickness of the irradiated foil (Figure 4 (a)). Thus, as a dislocation glides through a planar section of the irradiated layer (Figure 4 (b)), it will encounter only a certain proportion of L_d^N , which we refer to here as ρ_d^N and compute as

$$\rho_d^N = \frac{L_d^N}{\left(\frac{D}{d}\right)} \quad (9)$$

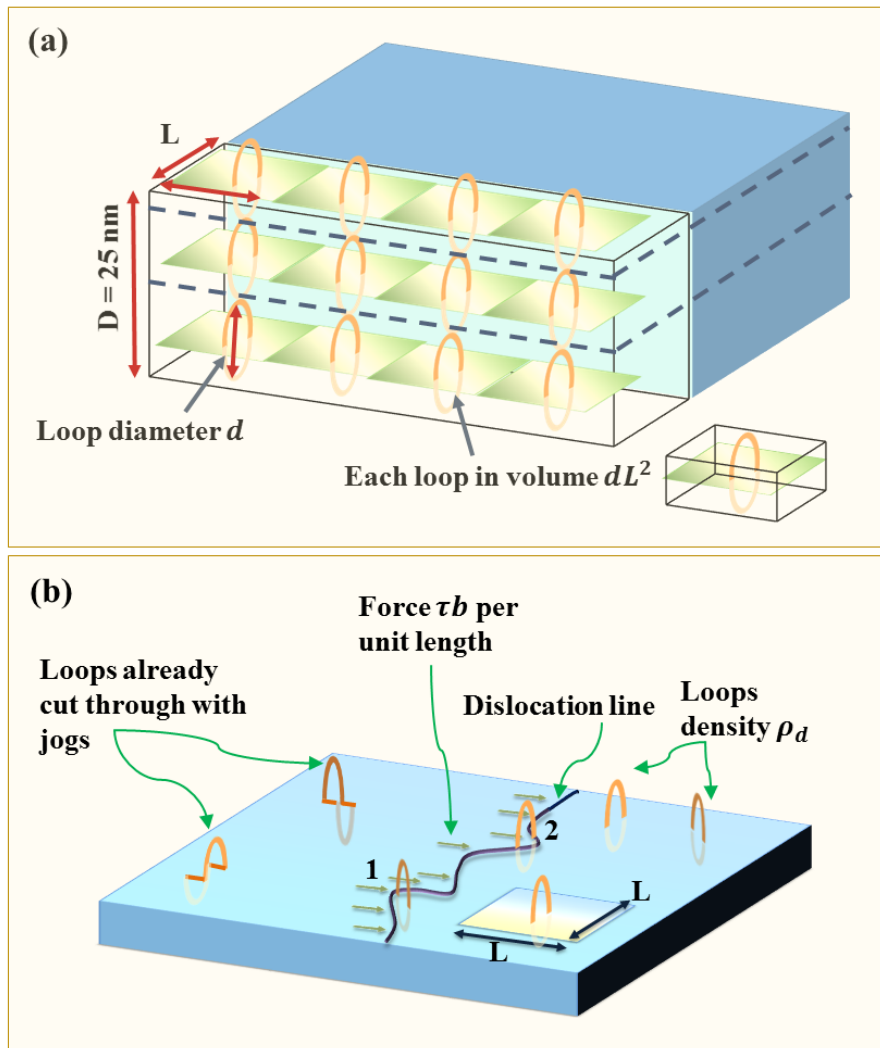


Figure 4 – (a) Schematic of ion-implanted TEM foil cross-section (thickness $D = 25 \text{ nm}$, the thickness of the implanted layer in Yi et al. (Yi et al., 2016)). Depicted are the assumptions made in the model of uniformly stacked loops with zero vertical spacing. (b) Illustration of dislocation glide through a planar section of the implanted layer, enclosed by the dashed line in (a). The glide plane is interspersed with implantation-induced loops (only few loops in the plane are illustrated here) that act as obstacles to the motion of the glide dislocation. Positions 1 and 2 show the glide dislocation interacting with a loop edge-on and face-on respectively.

Number of point defects in loop (N)	Frequency of creation of loop (f)	L_d^N (loops/m ²)	ρ_d^N (loops/m ²)
55.1	0.000359	1.96×10^{14}	1.58×10^{13}
126	0.000174	1.44×10^{14}	1.75×10^{13}
222	0.000115	1.26×10^{14}	2.04×10^{13}
344	3.72×10^{-5}	5.09×10^{13}	1.02×10^{13}
504	3.38×10^{-5}	5.59×10^{13}	1.36×10^{13}
679	1.13×10^{-5}	2.17×10^{13}	6.14×10^{12}
895	2.42×10^{-6}	5.34×10^{12}	1.73×10^{12}
1110	1.66×10^{-6}	4.08×10^{12}	1.47×10^{12}
1420	1.00×10^{-6}	2.78×10^{12}	1.14×10^{12}
		$L_{tot} = \sum L_d^N = \mathbf{6.07 \times 10^{14}}$	$\rho_{cut} = \sum \rho_d^N = \mathbf{8.81 \times 10^{13}}$

Table 2– Data extracted from TEM investigation of tungsten implanted tungsten of damage level 0.01 dpa (Yi et al., 2016) showing the density of loops of various sizes and the possibility of their encounter with gliding dislocations.

For each extracted data point from Figure 3, the calculated L_d^N and ρ_d^N are shown in Table 2. L_d^N summed over the range of loop sizes gives the total loop number density (L_{tot}) in the 25 nm thick implanted layer of the TEM foil (Table 2). $\sum \rho_d^N$ summed over the range of loop sizes gives ρ_{cut} , the number density of loops that will interact with a dislocation gliding through a plane in the implanted layer of the foil (Table 2), and that will contribute to τ_H^0 (i.e. the increased shear resistance of the implanted material).

We note here the ratio between ρ_{cut} and L_{tot} (Table 2) is $P = \rho_{cut}/L_{tot} = 0.0145$ (This ratio is specific to the 150 keV ion energy irradiation reported by Yi et al. (Yi et al., 2016)). We use this as a conversion factor to compute ρ_{cut} the loop number density intersecting a slip plane from the reported total loop number density (L_{tot}) for the other damage levels. While defect morphology may change with increasing dose, detailed knowledge of these changes is

difficult to ascertain. Thus, in order to minimise assumptions and fitting parameters in the model, we assume that P remains constant across all damage levels. This assumption implies that there is a linear scaling of the number density of loops of certain diameter (i.e. L_d^N for loops of diameter d and containing N point defects) with the total number density (i.e. L_{tot}) of loops, irrespective of the damage level.

The total loop number density (L_{tot}) has been reported by Yi et al. for a range of damage levels (Figure 7a in (Yi et al., 2016)). The reported values of L_{tot} for the damage levels 0.1, 0.32 and 1 dpa were extracted (Table 3). L_{tot} for 0.01 dpa is already known from Table 2. The corresponding ρ_{cut} is calculated as $\rho_{cut} = PL_{tot}$.

Damage Level (dpa)	L_{tot} (loops/m ²)	ρ_{cut} (loops/m ²)	τ_H^0 (MPa)
0.01	6.07×10^{14}	8.81×10^{13}	260
0.1	3.16228×10^{15}	4.59352×10^{14}	588
0.32	4.21697×10^{15}	6.12556×10^{14}	679
1	5.37032×10^{15}	7.80092×10^{14}	766

Table 3 – The implantation-induced additional shear resistance force to dislocation glide τ_H^0 computed for the different damage levels based on the defect density of loops as estimated from TEM of the damage microstructure in 150 eV W^r implanted tungsten by Yi et al. (Yi et al., 2016).

To derive τ_H^0 as a function of ρ_{cut} , a segment of a gliding dislocation of length L is considered to be moving through the planar section which is intersected by ρ_{cut} loops/m² (Figure 4(b)). Each loop is considered to be occupying a planar area of L^2 i.e. $\rho_{cut} = 1/L^2$

As the gliding dislocation cuts through the “forest” of implantation-induced loops, it displaces material above the slip plane, creating jogs in the cut dislocation loops. A model is considered here where the gliding dislocation may encounter a loop edge-on (Figure 4(b) position 1) or face-on (Figure 4(b) position 2), or in a position in between these two.

We note here that the mechanism of interaction between dislocations and loops may change as a function of the loop diameter. In future, equations accounting for such detailed interactions can be developed through dislocation dynamics studies of a progressively evolving loop-dominated microstructure. For simplicity, we here assume the same mechanism of interaction between dislocations and loops of all sizes and the effect of loop size is accounted for in the computation of ρ_{cut} (Table 2).

For edge-on loop interactions, one jog is created (equivalent to cutting through one dislocation in a dislocation forest). The length of the jog is equal to the Burgers vector magnitude b . Thus, the total energy required for the dislocation to cut through is equal to the energy needed to create the jog i.e. $Gb^2b/2$, where G is the shear modulus. The force driving the dislocation segment forward is $\tau_H^0 bL$. Thus the work done in moving the dislocation forward by a distance b is $(\tau_H^0 bL)b$. Equating energy with the work done gives

$$\tau_H^0 b^2 L = Gb^3/2 \quad (10)$$

Therefore,

$$\tau_H^0 = \frac{Gb}{2L} \quad (11)$$

Eq. (12) can be re-written by expressing L in terms of ρ_{cut}

$$\tau_H^0 = \frac{Gb}{2} \sqrt{\rho_{cut}} \quad (12)$$

Eq. (13) computes τ_H^0 for edge-on loop encounter where one jog is created at a time. In the case of a face-on loop interactions, the dislocation will have to create two jogs simultaneously

to cut through the loop, i.e. in this case $\tau_H^0 = 2 \frac{Gb}{2} \sqrt{\rho_{cut}}$. For small loops with $r \ll L$ this may be a more accurate approximation. In the general case of loop encounter with a dislocation, we can then re-write Eq. (13) as

$$\tau_H^0 = m \frac{Gb}{2} \sqrt{\rho_{cut}} \quad (13)$$

where $1 \leq m \leq 2$ is a pre-factor which accounts for the face-on or edge-on nature of dislocation-loop interaction. In other words, m represents the average barrier strength of the implantation-induced loops. $m = 1.23$ was obtained from fitting to the experimental result of the 0.01 dpa sample, and kept constant for simulations of the other damage levels. Using this and the respective ρ_{cut} values for each damage level as computed in Table 3, τ_H^0 for each damage level is computed (Table 3).

5. Results & Discussion

For purposes of direct comparison, the simulation and experimental results are plotted in the same coordinate frame and using the same colour and length scales.

5.1. Mechanical response from nano-indentation

Figure 5 (a) shows the measured load-displacement curves from nano-indentation of $\langle 001 \rangle$ oriented grains in the self-ion implanted tungsten samples exposed to different damage levels. One measurement was made in the unimplanted sample. Each of the other curves is the average of three different indents in each sample. The initial Hertzian elastic response in the curves in Figure 5(a) is almost identical in the unimplanted and implanted samples. This behaviour is expected since ion-implantation-induced changes in elastic modulus are small (Duncan et al., 2016; Hofmann et al., 2015b). The unimplanted sample, shows a large pop-in event at ~ 60 nm penetration depth. This is indicative of the onset of

plastic deformation and associated nucleation of dislocations (Ma et al., 2012). However, no such obvious pop-ins are observed in any of the implanted samples. This implies that while the unimplanted material is relatively defect free, the implanted samples, populated by implantation-induced defects, allow an easier nucleation of initial glide dislocations.

With increasing indentation depth, the implanted samples reach a noticeably higher load than the unimplanted material. This is consistent with the well-known hardening effect induced by irradiation defects, which has been previously reported in tungsten as well as other self-ion implanted materials, e.g. iron and iron alloys (Armstrong et al., 2011; Gibson et al., 2015; Hardie et al., 2015). The early saturation of this hardness increase, on the other hand, is surprising. Tracing the increase in hardness with irradiation, the 0.01 dpa sample shows a ~9% increase, 0.018 dpa sample ~13% increase and the 0.032, 0.1, 0.32 and 1 dpa samples all show ~27% increase. The saturation of hardening as early as 0.032 dpa (Figure 5 (b)) is lower than previous observations of hardness saturating above 0.4 dpa in ion-implanted tungsten (implanted with self-ions at 300 °C) (Armstrong et al., 2013).

The saturation of hardness is also reflected in the morphology of the surface pile-up around indents. AFM was used to measure the indent morphologies in the unimplanted sample, the 0.01 dpa sample and three samples above the saturation threshold level, 0.1, 0.32 and 1 dpa. To ensure reproducibility of results, three indents in $\langle 001 \rangle$ grains were measured for each sample. Figure D.1 in Appendix D shows that the results are consistent. Figure 6 shows the AFM measurements for one of the indents from each sample. The indent in the unimplanted sample shows a shallow pile-up that extends quite far from the indent (up to about 6 μm), visible in the form of pile-up streaks along the $\{110\}$ directions. The pile-up

around the indents becomes more confined and increases in height as implantation damage increases. Beyond 0.1 dpa, there is little change in the pile-up profile.

This saturation effect implies a saturation of the underlying defect population. A similar saturation in defect densities was found through TEM studies on self-ion implanted tungsten, tungsten-5%-rhenium and tungsten-5%-tantalum (all implanted at 150 keV) beyond 0.4 dpa (Yi et al., 2016). It has been seen that with increase in dose > 0.4 dpa, loop dynamics change resulting in the formation of strings and larger finger loops. In the process, freshly nucleated loops are absorbed, stalling further defect accumulation (Yi et al., 2016). Similar observations of saturation of defect densities and evolution defect morphologies beyond 0.1 dpa has also been noticed in 150 keV self-ion implanted iron and iron-chromium alloys (Yao et al., 2008).

Interestingly our observations suggest that, despite changing defect morphology in the saturation region, the overall effect of irradiation-induced defects on glide dislocations does not change significantly. Rather the material hardness and surface pile-up, and consequently dislocation mobility, remain largely the same across the higher damage levels.

To further explore this observation, CPFEM was used to simulate nano-indentation for the unimplanted tungsten, 0.01 dpa sample and three damage levels at and above the saturation level, 0.1, 0.32 and 1 dpa. The surface profiles predicted by CPFEM are compared with the AFM measurements (Figure 6). Very good agreement is observed between the CPFEM and AFM measurements across all the samples. The confinement of deformation along the slip directions consistent with the crystallography of bcc tungsten is clearly captured, leading to the expected four-fold pile-up pattern (Wang et al., 2004). CPFEM also reproduces the significant confinement of pile-up and increase in pile-up height for damage levels (> 0.1 dpa), in good agreement with the experimental results.

The simulated load-displacement curves are superimposed as dotted lines on the respective nano-indentation measurements in Figure 5. The CPFEE predictions capture the saturation in load-curves, with the 0.32 and 1 dpa samples showing ~ 3% difference and the 0.1 dpa sample, showing a 7% difference to the experimental observations. Quantitative agreement between CPFEE predictions and experimental observations inspires some confidence in the hypothesis of strain softening and the exponential rate of softening adopted in the model (Eq. (5)). The primary limitation of this model is that the underlying dynamics of dislocation nucleation and evolution are not accounted for. While this allows the model to have a minimal number of parameters, it renders it incapable of simulating features such as the pop-in in the unimplanted sample. However, despite this limitation, the model captures the implantation-induced changes in quite well.

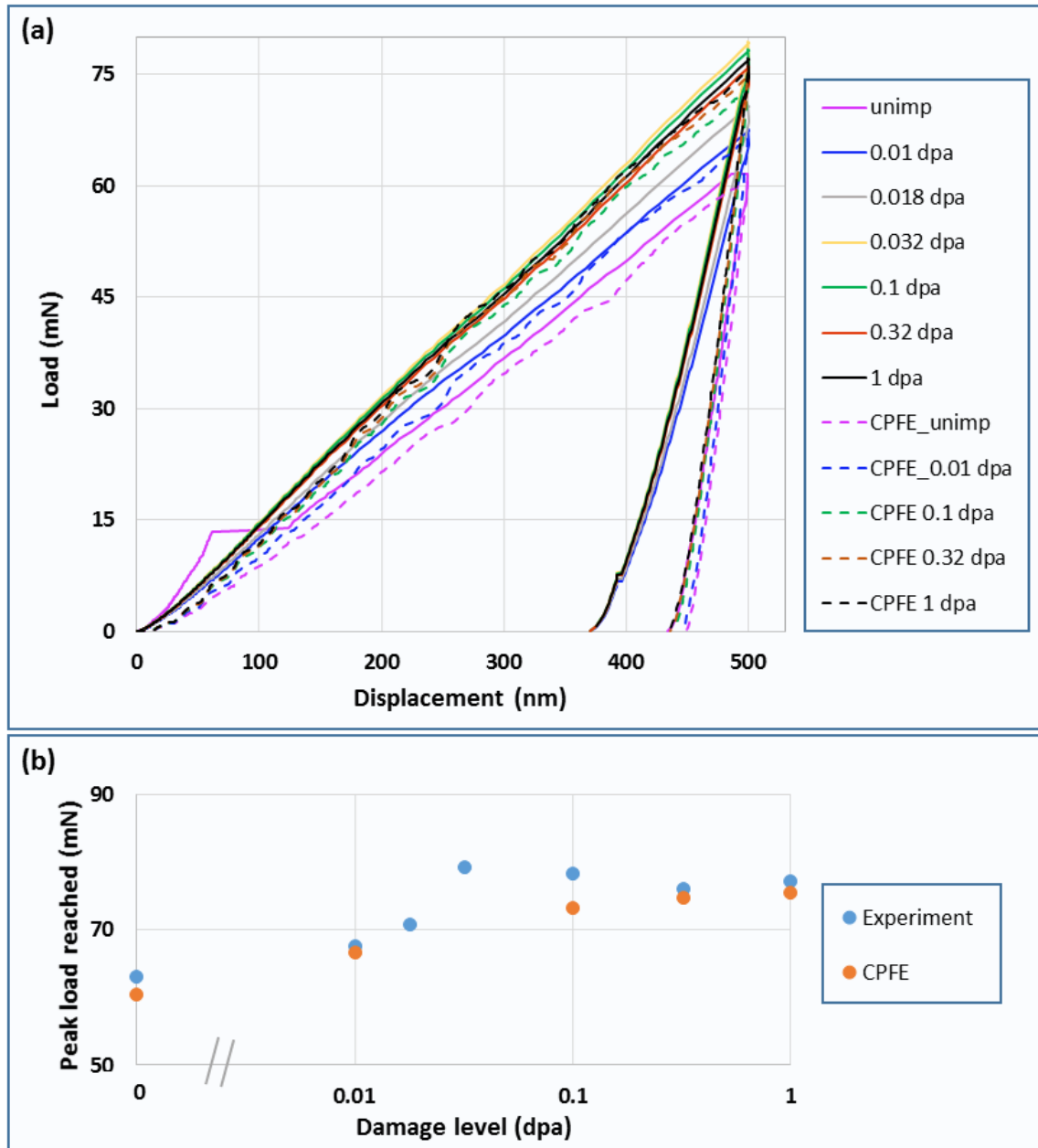


Figure 5 – (a) Load-displacement curves as measured by nano-indentation and predicted by CPFE for $\langle 001 \rangle$ -oriented grains in self-ion implanted samples with a range of damage levels (0 – 1 dpa). The solid curves are the average of three measurements done on three different indents in each sample. (b) Plot of peak load reached by the ion-implanted samples with different damage levels as measured by nano-indentation and predicted by CPFE. We note that CPFE simulates indentation for only 5 damage levels, excluding 0.018 and 0.032 dpa.

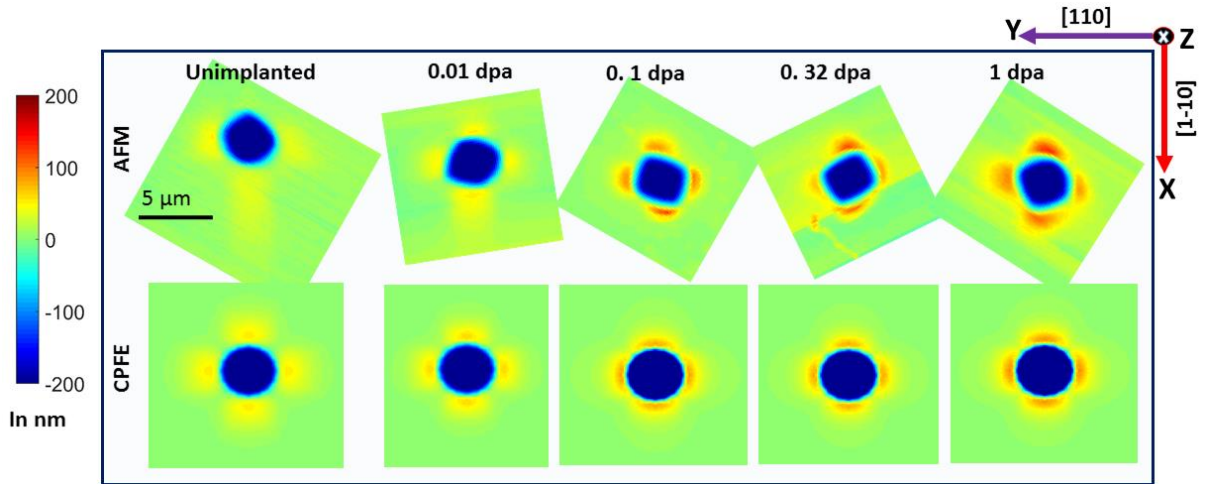


Figure 6 – Surface morphologies (height profile) of nano-indentations in pure tungsten and in self-ion implanted tungsten with varying damage levels as predicted by CPFE and measured by AFM after indentation. The AFM micrographs have been rotated to have the same in-plane orientations as the CPFE model. The surface normal pointing out of the page is along $[00-1]$.

5.2. Lattice distortions and GND density around indents

In addition to changes in indentation load-displacement curves and pile-up morphology, it is interesting to consider how irradiation-induced defects modify the lattice distortions and GND density distribution near indents. Here the two extremes, the unimplanted and the 1 dpa sample, are considered in detail. Lattice distortions around indents in both samples were probed using HR-EBSD. The experimental measurements are compared to the corresponding CPFE simulations, examining both residual lattice rotations and elastic lattice strains.

The indentation-induced change in orientation \mathbf{R} , for each point with final lattice orientation at time t , \mathbf{R}_t was calculated as (Suchandrima Das et al., 2018a):

$$\mathbf{R}_t = \mathbf{R}\mathbf{R}_0 \quad (14)$$

$$\mathbf{R} = \mathbf{R}_t\mathbf{R}_0^{-1} \quad (15)$$

where, \mathbf{R}_0 is the orientation of the un-deformed material. For CPFE, \mathbf{R}_0 was the original input orientation. For HR-EBSD \mathbf{R}_0 was taken as the average orientation of points far from the indent (25 μm away). Following the convention adopted in (Slabaugh, 1999), \mathbf{R} captures the

combined effect of sequential rotation about the X, Y and Z axis by the lattice rotation angles θ_x , θ_y and θ_z .

The deviatoric component of the residual elastic strain measured by HR-EBSD (Wilkinson, 1996) is compared with CPFE predictions. The deviatoric part of the CPFE predicted elastic strain ($\boldsymbol{\varepsilon}_{dev}^e$) was extracted as

$$\boldsymbol{\varepsilon}_{dev}^e = \boldsymbol{\varepsilon}^e - \boldsymbol{\varepsilon}_{vol}^e = \boldsymbol{\varepsilon}^e - 1/3 \text{Tr}(\boldsymbol{\varepsilon}^e)\mathbf{I} \quad (16)$$

where $\boldsymbol{\varepsilon}_{vol}^e$ is the volumetric strain.

Figure 7 (a) and (b) show the CPFE predictions of lattice rotations and all six components of the residual elastic deviatoric lattice strain for the unimplanted and the 1 dpa sample respectively. The corresponding measurements by HR-EBSD are shown in Figure 7 (c) and (d) respectively. The plots in Figure 7 show the XY plane i.e. the sample surface. HR-EBSD shows that in comparison to unimplanted tungsten, the magnitude of lattice strain and rotation is higher in the 1 dpa sample (particularly evident in ε_{xx} and in ε_{yy}), but the fields are also spatially more confined. This confinement is particularly prominent in ε_{xy} , ε_{zz} strain components and the lattice rotation fields. The CPFE captures this localisation of the elastic fields well.

CPFE predictions of implantation-induced change in magnitude and localisation of lattice distortions is particularly noticeable for the lattice rotations and strains ε_{xy} and ε_{zz} . The pattern of negative and positive lobes for these components also agrees very well with HR-EBSD measurements. Shear strains are generally more difficult to measure than the direct components of strain (Villert et al., 2009). In this case however, HR-EBSD measurement and CPFE prediction of the in-plane shear strain ε_{xy} , is surprisingly consistent, including the similarity in irradiation-induced changes in magnitude and confinement. Little change is

predicted by CPFÉ for the out-of-plane shear strains in both samples (which, as expected, are also much smaller than the other strain components), consistent with observations from HR-EBSD.

As lattice rotations are expected to play a dominant role in the overall deformation gradient (Nye, 1953), their distribution below the indents is also explored. Since HR-EBSD measurements are restricted to the indent surface, this is done exclusively through CPFÉ simulations. Figure 8 shows the lattice rotations beneath the indents, predicted by CPFÉ, for the unimplanted and the 1 dpa sample. They are plotted on virtual YZ slices at three points: At the indent centre (slice 2 in Figure 8) and 6 μm on either side of the indent centre (slices 1 and 3 in Figure 8). The steep strain gradients immediately below the indent make the analysis of the rotation field in slice 2 difficult. The differences in rotation fields becomes clearer by comparing slices 1 and 3. Here it is seen that the rotation fields in the 1 dpa sample are slightly smaller in magnitude and more confined than in the unimplanted material. This is particularly noticeable for θ_x and θ_z and confirms the 3D confinement of deformation in the 1 dpa sample.

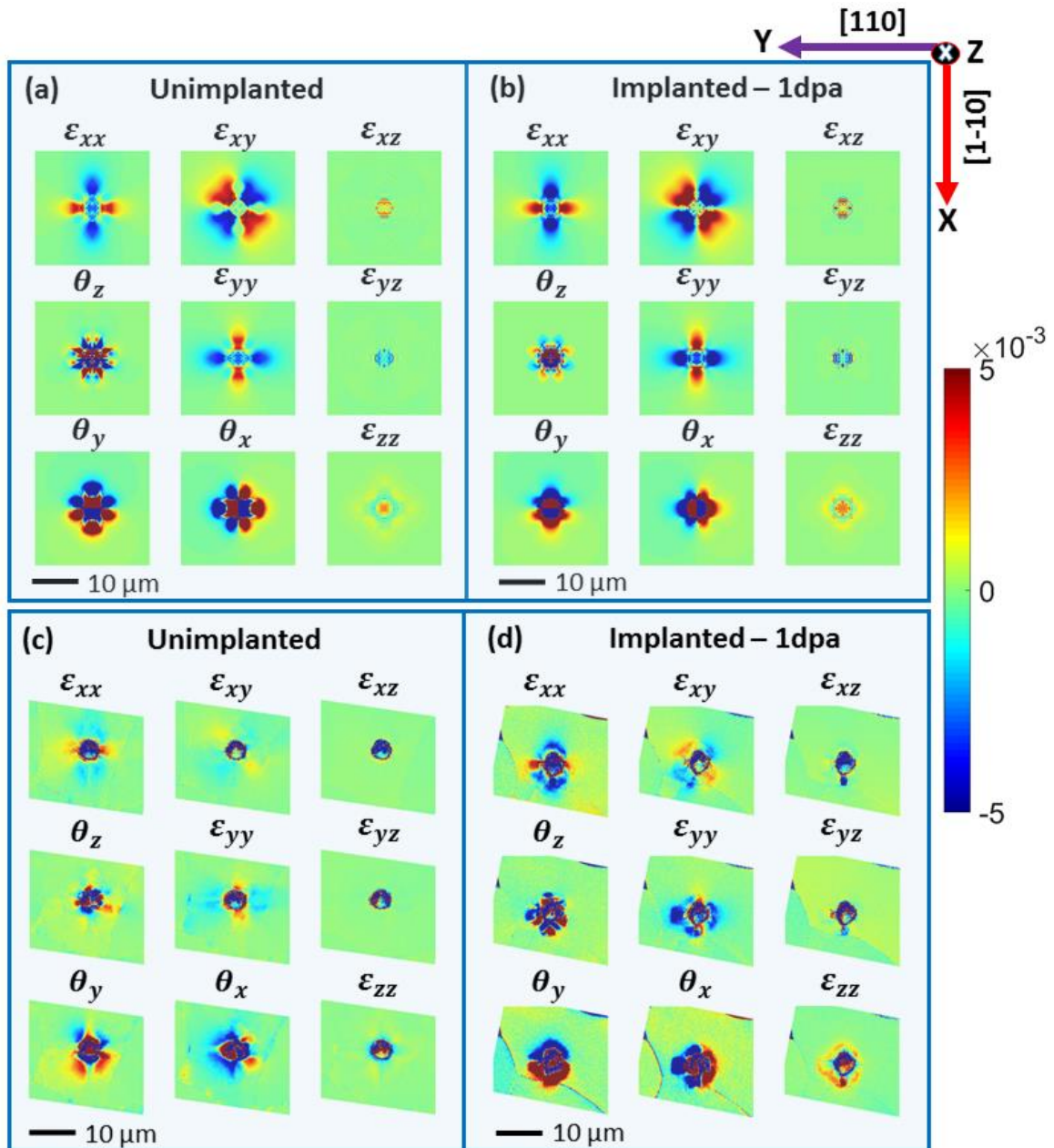


Figure 7—CPFE predictions of lattice rotations and all six components of the residual elastic deviatoric lattice strain plotted on the XY plane (sample surface) for the (a) unimplanted sample and (b) 1 dpa sample. HR-EBSD measurement of lattice rotations and all six components of the residual elastic deviatoric lattice strain plotted on the XY plane (indent surface) for the (c) unimplanted sample and (d) 1 dpa sample.

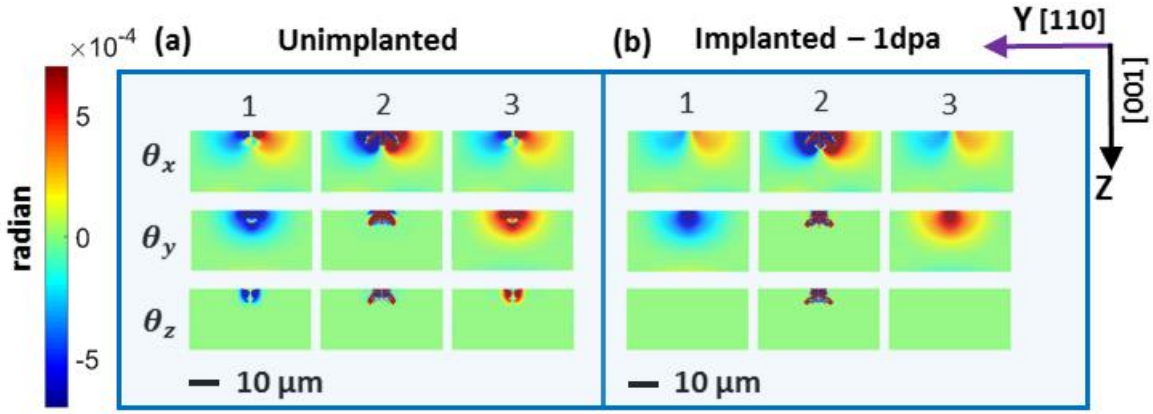


Figure 8 – CPFE predictions of the lattice rotations underlying the indents for the (a) unimplanted sample and (b) the 1 dpa sample. The lattice rotations are plotted on virtual YZ slices where slice 2 is at the indent centre and slices 1 and 3 represents the YZ cross-sections 6 μm on either side of the indent centre. The lattice rotations measurements are shown in radian.

The observations in Figure 7 and Figure 8 show that in the presence of irradiation damage, the applied deformation is accommodated in a more confined zone compared to the pristine sample. This implies that the effective strain gradient in the irradiated sample will be steeper than in the unirradiated case. The lattice curvature required to accommodate the strain gradient is provided by distribution of geometrically necessary dislocations (GNDs) (Fleck and Hutchinson, 1997). Steeper strain gradient suggest a higher density of GNDs. It has been argued that GNDs play an important role in the nucleation of cracks (Chen et al., 2017; Stroh, 1957; Wan et al., 2014) and possibly in crack propagation through crack tip blunting (Jiang et al., 2016). Thus, considering that this dislocation based stored energy could be useful criterion in determining material failure, we investigate the GND distribution in the irradiated sample and its variation with dose.

Details of the GND density computation can be found elsewhere (Suchandrima Das et al., 2018a) and in Appendix E. Here we use the L2 minimisation technique, which minimizes the sum of squares of the dislocation densities (ρ), i.e. $\sum_j \rho_j^2 = \rho^T \rho$, to compute the total GND density summed over the twelve $a/2\langle 111 \rangle \{110\}$ slip systems considered here (Marichal et al.,

2013; Srivastava et al., 2013)). We assume that dislocations are either of pure edge or pure screw type, resulting in 16 dislocation types in total (Suchandrima Das et al., 2018a).

The GND density produced across all slip systems as measured by HR-EBSD (Birosca et al., 2019; Chen et al., 2017; Zhu et al., 2017) and computed by CPFE is compared for the unimplanted, 0.01, 0.1, 0.32 and 1 dpa samples (Figure 9).

We note that the absolute values of GND densities calculated by the two techniques (HR-EBSD and CPFE) differ. This is because of the different step size and mesh size used respectively. Owing to the lack of inherent length scale in plasticity, the step size or mesh size is directly representative of the considered Burgers circuit size. GNDs are the excess dislocations stored within the Burgers circuit that are required to accommodate the lattice curvature (Ashby, 1970). With reduction in step size (or Burgers circuit size) the fraction of dislocations that appear as GNDs increases (more dipoles are resolved as GNDs) until finally, for Burgers' circuit smaller than the dipole size, every dislocation appears as a GND. Thus the density of GNDs increases with decreasing step size, as shown by Jiang et al. in simulations of a deformed copper polycrystal (Jiang et al., 2015, 2013). The mesh size in CPFE was chosen to ensure there is no mesh dependence, with a smallest element size of 50 nm near the indenter tip. The step size in HR-EBSD (169 nm) was chosen to ensure that the resolution is sufficient to resolve strain gradients near indents, while reducing the measurement noise.

The trend in GND density distribution as a function of increasing irradiation damage predicted by CPFE agrees quite well with the HR-EBSD measurement on the sample surface Figure 9. A clear trend of confinement of the GND density field is evident with increasing damage dose up to 0.1 dpa. Beyond 0.1 dpa, there is little the change in the GND density distribution, which is consistent with the mechanical response observed in Figure 5 and the observations of the

indent surface profile Figure 6. The confinement of the GND density field beneath indents follows the same trend, as shown by the CPFE predicted GND density plots on the XZ and YZ cross-sections through the indent (Figure 1 (b) for reference co-ordinate frame) in Figure E.1 in Appendix E.

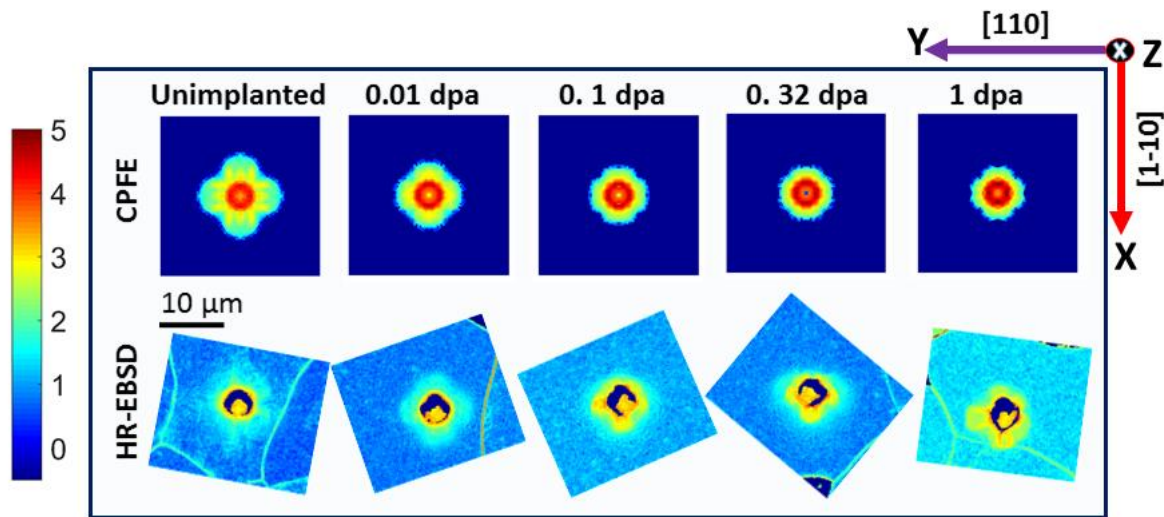


Figure 9 – Sum of GNDs (ρ) over all slip systems as predicted by CPFE and measured by HR-EBSD for the self-ion implanted tungsten samples of the varying damage levels. The GNDs on each of the 12 slip systems were computed using L2 minimisation. The plots are shown on the sample surface i.e. on the XY cross-section. The same colour scale is used for all plots showing $\log_{10}(\rho)$ with ρ in $1/\mu\text{m}^2$. The HR-EBSD maps are rotated to have the same in-plane orientation as in the CPFE model.

A notable difference between the HR-EBSD-measured and CPFE-predicted GND density distribution is the appearance of pronounced “lobes” around the indents in the higher damage levels (see HR-EBSD measurement of 1 dpa sample). Such lobe formation may be due to the evolution of defect morphologies at higher damage levels, as captured in the experimental HR-EBSD measurements. While CPFE accurately captures the localisation of deformation at the higher dose levels, the lack of integrated dislocation dynamics renders the model incapable of simulating the lobe formation as experimentally observed for example in the 1 dpa sample. Advanced CPFE models with integrated dislocation defect interactions are

currently being developed by various groups. Examples of such models have been reported by Li et al. to simulate irradiation hardening in iron single crystal (Li et al., 2014) and by Ohashi et al. who simulated scale dependent characteristics of mechanical properties of polycrystals (Ohashi et al., 2007). However to account for the increased complexity of the microstructure, an increase in the number of assumptions and fitting parameters is unavoidable.

The current simulations and experimental provide clear evidence for irradiation induced softening in self-ion implanted tungsten. The CPFEM model captures the variation of mechanical properties across a range of damage levels, including damage saturation. Importantly, it does so with a minimal number of fitting parameters: τ_H^0 is based on TEM observations, and γ and k are kept constant across all damage levels (fitted to the 0.01 dpa experimental result). Interestingly, the formulation closely follows the strain softening formulation adopted to simulate helium-implantation damage in tungsten (Suchandrima Das et al., 2018b). It is surprising that this relatively simple formulation is sufficiently general to allow the effects of vastly different damage microstructures (induced by helium and self-ion bombardment) to be simulated with good agreement with experimental results. There are a number of improvements that could be made, for e.g. accounting for the contribution of defects too small to be resolved by TEM. Also insights drawn from atomistic and/or dislocation dynamics simulations that can give detailed information about the interaction between gliding dislocations and loops of varying sizes and morphologies (i.e. a more precise estimate of the obstacle strength and how its overcome) would further improve the accuracy of the model.

Despite the limitations, the current model provides an effective and straightforward means of exploring the impact of ion-induced damage on dislocation-mediated plastic slip as

a function of dose. It triggers a promising idea whereby, minimal parameters derived from experimental observations from a small sample of the irradiated reactor component (e.g. TEM observations shedding light on neutron-irradiated loop concentration and estimates of the helium concentration) could be used in such predictive models to predict the anticipated macroscopic properties.

5.3. Translating small-scale response to predict macroscopic behaviour

Having verified the accuracy of the CPFÉ model for self-ion implanted tungsten, it can be used to predict the macroscopic deformation behaviour of a similarly irradiated, polycrystalline bulk material. To do this we generated a polycrystalline cube ($120 \times 120 \times 120 \mu\text{m}^3$) in Abaqus, with 512 cubic grains as shown in Figure 10 (a). Each grain was assigned a random crystallographic orientation and the elastic material properties of tungsten (see Appendix B). The bottom of the cube was kept fixed and symmetric boundary conditions were applied on the XY and YZ faces. The cube was meshed with C3D20R elements such that each grain was assigned 64 elements, giving a total mesh size of 32768 elements. Uniaxial compression tests were simulated by displacing the top surface in the negative Y-direction by $6 \mu\text{m}$ (5% strain applied). Crystal plasticity was integrated into the simulation by calling the previously developed UMAT at every Gauss point. The simulations were carried out for 0.01, 0.1, 0.32 and 1 dpa damage levels, by using the relevant τ_H^0 in the CPFÉ model in each case (Table 3 shows the dose-dependence of τ_H^0). All other CPFÉ parameters are dose independent and are provided in Appendix C). σ_{yy} and U_{yy} (displacement in the Y direction) were extracted from all nodes of each element, for each time increment. At each time increment, the average compressive stress was considered to be $\sigma = \sum_n \sigma_{yy}/n$ where n is the number of nodes. U_{yy}

and the original dimension of the cube ($L = 120 \mu\text{m}$) were used to compute the true strain at each time increment as $\epsilon = \ln\left(\frac{L+U_{yy}}{L}\right)$. The resultant compressive stress-strain curves predicted at each dose are shown in Figure 10 (b).

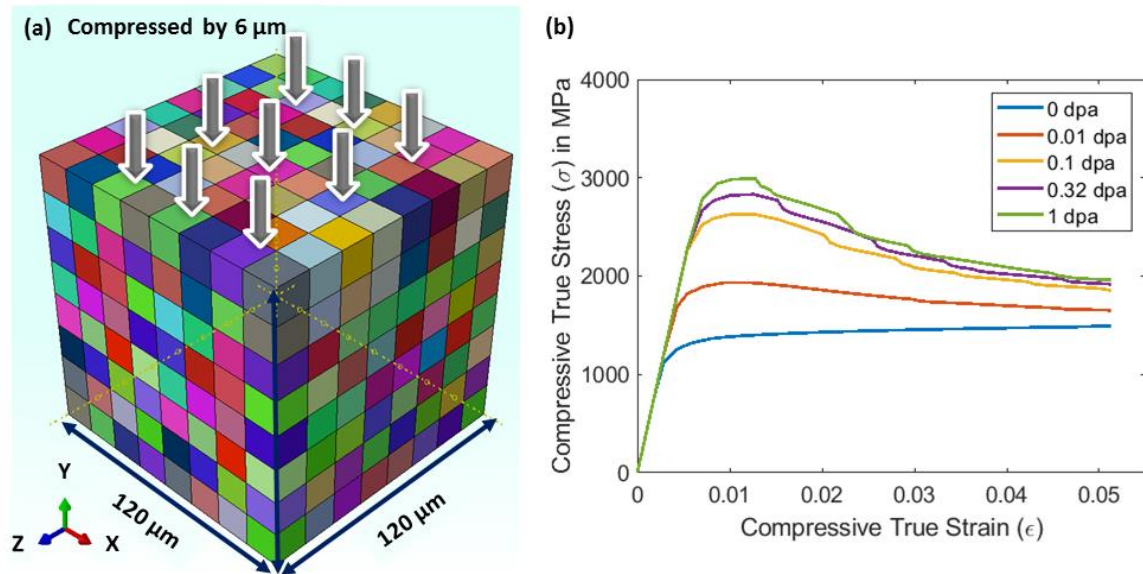


Figure 10 – (a) Polycrystalline cube generated in Abaqus with 512 grains, each of which was assigned a random crystallographic orientation. (b) Macroscopic stress-strain curves generated by uniaxial compression testing of the polycrystalline cube. To generate each curve, the cube was assigned the crystal plasticity material model of self-ion implanted tungsten exposed to a particular damage level.

The curves in Figure 10 (b) clearly show both irradiation-induced hardening and strain-softening increasing with dose and saturating beyond 0.1 dpa. With this established crystal plasticity material model, further tests, such as cyclic loading of such polycrystalline irradiated materials, may be simulated to assess their fatigue life (Korsunsky et al., 2007) or thermo-mechanical analysis at fusion relevant steady/transient heating loads (Fukuda et al., 2015; Li et al., 2017) may be performed. Such predictions, made as a function of evolving dose, could then be integrated into the reactor design to ensure property evolution is correctly accounted for when assessing long-term serviceability of components.

6. Conclusion

Understanding the impact of in-service radiation damage on structural and functional material properties is vital for the design of future fusion reactors. Estimating macroscopic properties is challenging as ion-implanted samples, used to mimic neutron irradiation, are only a few microns thick. Here we have demonstrated how experimental characterisation data from ion-implanted samples can be used to predict the anticipated macroscopic mechanical properties using a two-step process: First we develop a mesoscale material model that captures the physics of the irradiation damage. The numerical formulation for the material model is based on and validated against a combination of experimental observations on ion-implanted samples. This material model is then used to simulate the macroscopic deformation behaviour of similarly irradiated polycrystalline bulk material.

We have used self-ion implanted tungsten as a prototypical material to demonstrate this process. The results allow the following conclusions to be drawn about the dose-dependent deformation behaviour self-ion-implanted tungsten:

- Surface profiles of indents in self-ion implanted samples may show pile-up or suppression of pile-up as a function of grain orientation. In self-ion-implanted tungsten the largest pile-up occurred in $\langle 001 \rangle$ oriented grains, similar to observations made in helium-implanted tungsten.
- Pile-up around indents in $\langle 001 \rangle$ grains increased with increasing damage level and reached a saturation beyond 0.032 dpa.
- A similar saturation is observed in the mechanical response, captured by nano-indentation load-displacement curves. The maximum load increases by $\sim 27\%$ for damage levels between 0.032 and 1 dpa.

- Irradiation induced hardening accompanied by surface pile-up and slip step formation, indicates that irradiation defects initially act as strong obstacles to glide dislocations, but that their obstacle strength is reduced with increasing plastic deformation. A CPFÉ formulation built on this hypothesis correctly predicts indentation load and indent surface profiles for unimplanted, 0.01, 0.1, 0.32 and 1 dpa samples. The shear resistance of irradiation defects in CPFÉ is physically-based and derived from TEM observations. Only two parameters are fitted to the experimental results of the 0.01 dpa sample and kept constant for all other damage levels.
- Confinement of the deformation field is explored in detail by comparing the unimplanted and the 1 dpa sample. CPFÉ predictions of residual lattice rotations and lattice strains around the indents are in good agreement with HR-EBSD measurements.
- CPFÉ and HR-EBSD computed GND density fields around the indents, across a range of damage levels, show similar trends: deformation becomes increasingly confined with rising damage level up to 0.1 dpa. Beyond this little change is noticed.
- The CPFÉ model was successfully used to predict the macroscopic deformation behaviour of self-ion irradiated polycrystalline tungsten. The macroscopic stress-strain curves show initial irradiation-induced hardening, followed by strain-softening during deformation. Similar to the small-scale behaviour, irradiation induced changes were seen to increase as a function of dose and saturate beyond 0.1 dpa.

Acknowledgements

We thank A.J. Wilkinson for providing the software for HR-EBSD analysis. This work was funded by Leverhulme Trust Research Project Grant RPG-2016-190. ET acknowledges financial support from the Engineering and Physical Sciences Research Council Fellowship grant EP/N007239/1. Electron and atomic force microscopy were performed at the David Cockayne Centre for Electron Microscopy, Department of Materials, and at the LIMA lab, Department of Engineering Science, both at the University of Oxford. Ion implantations were performed at the Helsinki Accelerator laboratory, Department of Physics, University of Helsinki.

Appendix A

Sample (grain is <001> unless mentioned otherwise)	Euler Angles ($\varphi_1, \varphi, \varphi_2$) ³	Out-of-plane orientation	Misorientation with <111> ,<110> or <001> (in degrees)
Unimplanted grain 1	277.8,5.4,83	[9.34,1.15,99.56]	5.4
Unimplanted grain 2	71.8,10.5,23.4	[7.24,16.72,98.33]	10.5
Unimplanted grain 3	180.9,6.6,29.6	[5.68,9.99,99.34]	6.6
Unimplanted grain 4 <011>	254.5,39.7,6.8	[7.56,63.43,76.94]	6.99
Unimplanted grain 5 <111>	330.3,43.5,61.6	[60.55,32.74,72.54]	16.78
0.01 dpa grain 1	214.7,1.6,293.3	[-2.56,1.1,99.96]	1.6
0.01 dpa grain 2	33.7,2.4,176.4	[0.26,-4.18,99.91]	2.4
0.01 dpa grain 3	51.2,9.1,159	[5.67,-14.77,98.74]	9.1
0.018 dpa grain 1	190.3,5.4,21	[3.37,8.79,99.56]	5.4
0.018 dpa grain 2	289,7.8,69	[12.67,4.86,99.07]	7.8
0.018 dpa grain 3	213.4,11.2,15.8	[5.29,18.69,98.1]	11.2
0.032 dpa grain 1	268.3,9.6,92	[16.67,-0.58,98.6]	9.6
0.032 dpa grain 2	185.8,3.2,19	[1.82,5.28,99.84]	3.2
0.032 dpa grain 3	13.4,5.8,198.2	[-3.16,-9.6,99.4]	5.8
0.1 dpa grain 1	27.8,3.2,181.1	[-0.11,-5.58,99.8]	3.2
0.1 dpa grain 2	16.3,7.4,200	[-4.41,-12.1,99.1]	7.4

³ The Euler angle convention used is as follows: $Z1 = \begin{bmatrix} \cos \varphi_1 & \sin \varphi_1 & 0 \\ -\sin \varphi_1 & \cos \varphi_1 & 0 \\ 0 & 0 & 1 \end{bmatrix}$; $X = \begin{bmatrix} 1 & 0 & 0 \\ 0 & \cos \varphi & \sin \varphi \\ 0 & -\sin \varphi & \cos \varphi \end{bmatrix}$; $Z2 = \begin{bmatrix} \cos \varphi_2 & \sin \varphi_2 & 0 \\ -\sin \varphi_2 & \cos \varphi_2 & 0 \\ 0 & 0 & 1 \end{bmatrix}$ and the rotation matrix $R = Z1 * X * Z2$.

0.1 dpa grain 3	162.1,4.1,341.8	[-2.23,6.79,99.74]	4.1
0.32 dpa grain 1	103.8,4.9,64.4	[7.7,3.69,99.63]	4.9
0.32 dpa grain 2	59.6,9.2,114.6	[14.54,-6.66,98.71]	9.2
0.32 dpa grain 3	344.1,10.8,230.3	[-14.42,-11.97,98.2]	10.8
1 dpa grain 1	126.5,7.6,67.4	[12.21,5.08,99.12]	7.6
1 dpa grain 2	319.8,7.1,87.9	[12.35,0.45,99.23]	7.1
1 dpa grain 3	207.5,5.1,0.4	[0.06,8.89,99.6]	5.1
1 dpa grain 4 <011>	263.7,42.8,82.4	[67.35,8.99,73.37]	5.7075
1 dpa grain 5 <111>	264.2,42.8,82.4	[58.07,37.43,72.3]	14.36

Table A.1 - List of the out-of-plane orientation of the chosen point in each sample grain and the misorientation of the chosen point with respect to the perfect <111>, <110> or <001> out-of-plane direction.

Appendix B

The stiffness of tungsten (material for sample block) is ~36% that of diamond (material of the indenter tip) (Table B.1). It has been seen from simulations using a rigid sharp indenter, that simulation results match the experimental results well if the results are scaled using an effective modulus, E_{eff} (M. Li et al., 2009)

$$P (exp.) = \frac{E_{eff} (exp.)}{E (FEA)} P(FEA) \quad (B.1)$$

Thus, to avoid a full meshing and increase in simulation size, the indenter was designed as a discrete rigid wire frame.

$E_{diamond}$	$E_{tungsten}$	$\nu_{diamond}$	$\nu_{tungsten}$	E_{eff}	$R_{indenter}$
1143 GPa	410 GPa	0.0691	0.28	322.58 GPa	4.2 μm

Table B.1 – Values of Young's modulus and Poisson's ratio for diamond (indenter tip) and tungsten (indented sample) as obtained from literature (Bolef and De Klerk, 1962; Featherston and Neighbours, 1963; Klein and Cardinale, 1993)⁴.

⁴ With the assumption of isotropic, linear elastic solid, the Young's modulus and Poisson's ratio are related to the elastic constant as follows: $E = c_{11} - 2 \left(\frac{c_{12}^2}{c_{11} + c_{12}} \right)$ and $\nu = c_{12} / (c_{11} + c_{12})$.

Appendix C

Material Property	Value	Reference
Elastic modulus E	410 GPa	(Ayres et al., 1975; Bolef and De Klerk, 1962; Featherston and Neighbours, 1963; Klein and Cardinale, 1993)
Shear modulus G	164.4 GPa	(Ayres et al., 1975; Bolef and De Klerk, 1962; Featherston and Neighbours, 1963; Klein and Cardinale, 1993)
Poisson's ratio ν	0.28	(Ayres et al., 1975; Bolef and De Klerk, 1962; Featherston and Neighbours, 1963; Klein and Cardinale, 1993)
Burgers' vector b	2.7×10^{-10} m	(Dutta and Dayal, 1963)
Activation energy ΔF	0.22 eV	Chosen to reduce strain-rate sensitivity
Boltzmann constant k	1.381×10^{-23} J/K	(Sweeney et al., 2013)
Temperature T	298 K	Room temperature assumed similar to experimental conditions
Attempt frequency ν	1×10^{11} s ⁻¹	Value chosen and kept fixed
Density of statistically stored dislocations, ρ_{SSD}	1×10^{10} m ⁻²	Section C.1
Density of mobile dislocations ρ_m	1×10^{10} m ⁻²	Section C.1
Probability of pinning Ψ	0.857×10^{-2}	Value chosen and kept fixed
τ_c^0	500 MPa	Fitted to experimental data of unimplanted sample
γ	0.08	Fitted to experimental data of 0.01 dpa sample and kept fixed for all other dose rates

C'	0.1	Fitted to experimental data of unimplanted sample
Average barrier strength of the implantation-induced loops m	1.23	Fitted to experimental data of 0.01 dpa sample and kept fixed for all other dose rates
τ_H^0 (0.01 dpa)	260	Derived based on TEM data
τ_H^0 (0.1 dpa)	588	Derived based on TEM data
τ_H^0 (0.32 dpa)	679	Derived based on TEM data
τ_H^0 (1 dpa)	766	Derived based on TEM data

Table C.1– List of parameters used in the constitutive law in the CPFÉ formulation and their corresponding values.

Section C.1: Determining values of ρ_{SSD} and ρ_m

In nano-indented pure tungsten, the GND density was found to be on the order of $\sim 10^{17} \text{ m}^{-2}$ by both Laue diffraction measurements and CPFÉ simulations (Suchandrima Das et al., 2018a). With reference to this, for the CPFÉ calculations here, we assume the SSD densities, ρ_{SSD} and ρ_m , to be much smaller than the GND density estimate, on the order of 10^{10} m^{-2} .

Appendix D

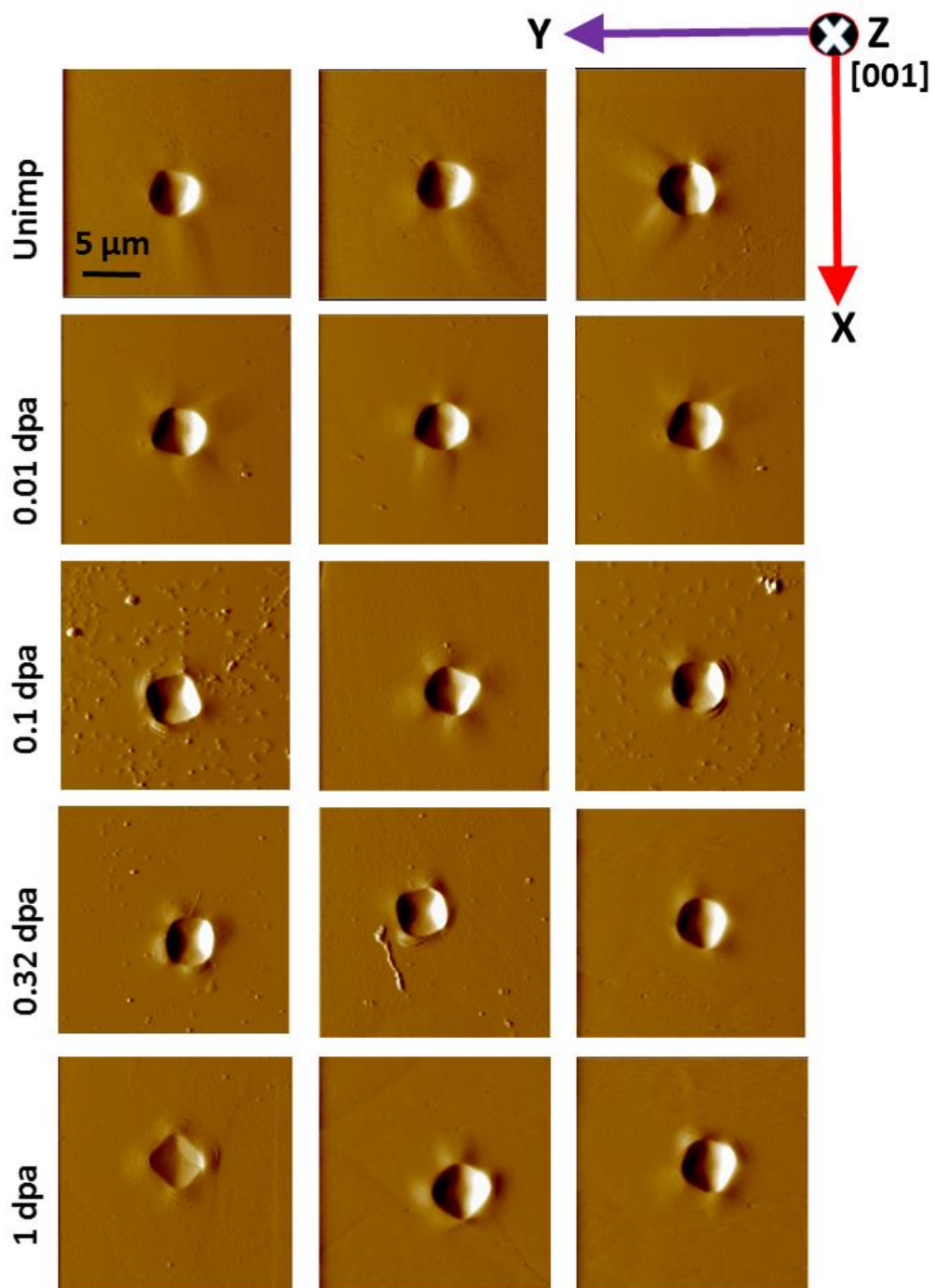


Figure D.1 – AFM gradient micrographs of indents in three $\langle 001 \rangle$ grains in self-ion implanted tungsten samples of varying damage levels.

Appendix E

GND density provides a useful measure of the combined effect of the lattice rotation and lattice strain. It is a direct function of the total plastic deformation gradient, \mathbf{F}^p (or elastic deformation gradient, \mathbf{F}^e) (Suchandrima Das et al., 2018a). Details of the GND density computation can be found elsewhere (Suchandrima Das et al., 2018a). Briefly, GND density, ρ is calculated by exploiting its relation with the closure failure ($\langle \mathbf{B} \rangle$) induced by plastic deformation in a material, where $\langle \mathbf{B} \rangle = \iint_S (\text{CURL}(\mathbf{F}^p))^T \mathbf{N} dS \cong \iint_S (-\text{CURL}(\mathbf{F}^e))^T \mathbf{N} dS$ (Nye, 1953). The relation can be defined as

$$\sum_{\lambda} (\mathbf{b}^{\lambda} \otimes \boldsymbol{\rho}^{\lambda}) = (\text{CURL}(\mathbf{F}^p))^T = (-\text{CURL}(\mathbf{F}^e))^T \quad (\text{E.1})$$

$$\cong (-\text{CURL}(\boldsymbol{\varepsilon}^e + \boldsymbol{\omega}^e))^T$$

where, \mathbf{b} is the Burgers' vector, λ is one of the n slip systems, CURL of any second-order tensor V is described by $(\nabla \times V)_{km} = \epsilon_{ijk} V_{mj,i}$ (Suchandrima Das et al., 2018a), $\boldsymbol{\varepsilon}^e$ is the residual elastic lattice strain and $\boldsymbol{\omega}^e$ is the residual lattice rotation. The 3×3 tensor obtained by calculating $(-\text{CURL}(\boldsymbol{\varepsilon}^e + \boldsymbol{\omega}^e))^T$, can be reshaped into a 9×1 column vector. $\boldsymbol{\rho}$ can be represented as a column vector representing densities of j dislocation types. Then Eq. E.1 can be re-written as

$$\mathbf{A}\boldsymbol{\rho} = \boldsymbol{\alpha} \quad (\text{E.2})$$

where \mathbf{A} is a linear operator ($9 \times j$ matrix, for j types of dislocations), where the j^{th} column contains the dyadic product of the Burgers' vector and line direction of the j^{th} dislocation type. Usually $j > 9$, and thus there is no unique solution for $\boldsymbol{\rho}$. Hence, an optimisation technique needs to be used to obtain $\boldsymbol{\rho}$. In a recent study it was seen that L2 minimisation, which minimises the sum of squares of dislocation densities i.e. $\sum_j \rho_j^2 = \boldsymbol{\rho}^T \cdot \boldsymbol{\rho}$, can reliably predict the sum of GNDs produced across all slip systems (Suchandrima Das et al., 2018a). Here we use this minimisation technique as we are concerned primarily with the sum of dislocation

densities produced across the considered slip systems ($a/2\langle 111 \rangle$ Burgers vector gliding on $\{110\}$ planes (Marichal et al., 2013; Srivastava et al., 2013)).

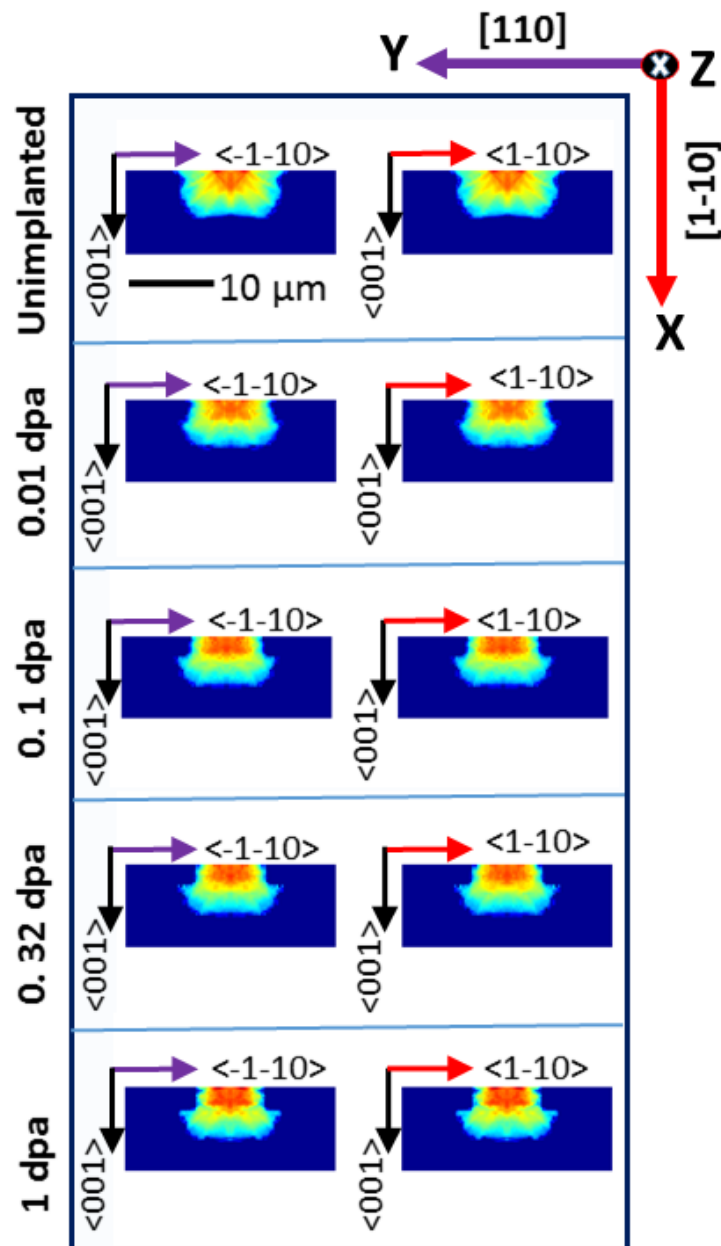


Figure E.1 - Sum of GNDs (ρ) over all slip systems as predicted by CPFЕ for the self-ion implanted tungsten samples of the varying damage levels. The GNDs on each of the 12 slip systems were computed by L2 minimisation. The XZ and YZ cross-sections of 3D field of GND sum around the indent, as predicted by CPFЕ, are shown for each sample. The same colour scale is used for all plots showing $\log_{10}(\rho)$ with ρ in $1/\mu\text{m}^2$. The XYZ coordinate system on the top right corner refers to the co-ordinate system used for the model and the experimental sample.

References

- Armstrong, D.E.J., Wilkinson, A.J., Roberts, S.G., 2011. Mechanical properties of ion-implanted tungsten–5 wt% tantalum. *Phys. Scr.* T145, 14076. <https://doi.org/10.1088/0031-8949/2011/T145/014076>
- Armstrong, D.E.J., Yi, X., Marquis, E.A., Roberts, S.G., 2013. Hardening of self ion implanted tungsten and tungsten 5-wt% rhenium. *J. Nucl. Mater.* 432, 428–436. <https://doi.org/10.1016/j.jnucmat.2012.07.044>
- Ashby, M.F., 1970. The deformation of plastically non-homogeneous materials. *Philos. Mag.* 21, 399–424. <https://doi.org/10.1080/14786437008238426>
- ASTM International, West Conshohocken, PA, 2009, U., 2009. ASTM E521–96(2009) e1, Standard Practice for Neutron Radiation Damage Simulation by Charged-Particle Irradiation.
- Ayres, R.A., Shannette, G.W., Stein, D.F., Roberts, S.G., Ahlgren, T., Antusch, S., Armstrong, D.E.J., Balden, M., Baluc, N., Barthe, M.-F., Basuki, W.W., Battabyal, M., Becquart, C.S., Blagoeva, D., Boldyryeva, H., Brinkmann, J., Celino, M., Ciupinski, L., Correia, J.B., De Backer, A., Domain, C., Gaganidze, E., García-Rosales, C., Gibson, J., Gilbert, M.R., Giusepponi, S., Gludovatz, B., Greuner, H., Heinola, K., Höschel, T., Hoffmann, A., Holstein, N., Koch, F., Krauss, W., Li, H., Lindig, S., Linke, J., Linsmeier, C., López-Ruiz, P., Maier, H., Matejicek, J., Mishra, T.P., Muhammed, M., Muñoz, A., Muzyk, M., Nordlund, K., Nguyen-Manh, D., Opschoor, J., Ordás, N., Palacios, T., Pintsuk, G., Pippin, R., Reiser, J., Riesch, J., Roberts, S.G., Romaner, L., Rosiński, M., Sanchez, M., Schulmeyer, W., Traxler, H., Ureña, A., van der Laan, J.G., Veleva, L., Wahlberg, S., Walter, M., Weber, T., Weitkamp, T., Wurster, S., Yar, M.A., You, J.H., Zivelonghi, A., 1975. Elastic constants of tungsten–rhenium alloys from 77 to 298 °K. *J. Appl. Phys.* 46, 1526–1530. <https://doi.org/10.1063/1.321804>
- Beck, C.E., Hofmann, F., Eliason, J.K., Maznev, A.A., Nelson, K.A., Armstrong, D.E.J., Armstrong, D.E.J., 2017. Correcting for contact area changes in nanoindentation using surface acoustic waves. *Scr. Mater.* 128, 83–86. <https://doi.org/10.1016/j.scriptamat.2016.09.037>
- Becquart, C.S., Domain, C., 2009. An object Kinetic Monte Carlo Simulation of the dynamics of helium and point defects in tungsten. *J. Nucl. Mater.* 385, 223–227. <https://doi.org/10.1016/j.jnucmat.2008.11.027>
- Birosca, S., Liu, G., Ding, R., Jiang, J., Simm, T., Deen, C., Whittaker, M., 2019. The dislocation behaviour and GND development in a nickel based superalloy during creep. *Int. J. Plast.* 118, 252–268. <https://doi.org/https://doi.org/10.1016/j.ijplas.2019.02.015>
- Bolef, D.I., De Klerk, J., 1962. Elastic Constants of Single-Crystal Mo and W between 77° and 500°K. *J. Appl. Phys.* 33, 2311–2314. <https://doi.org/10.1063/1.1728952>
- Britton, T.B., Hickey, J.L.R., 2018. Understanding deformation with high angular resolution electron backscatter diffraction (HR-EBSD). *IOP Conf. Ser. Mater. Sci. Eng.* 304, 12003.
- Chen, B., Jiang, J., Dunne, F.P.E., 2017. Is stored energy density the primary meso-scale mechanistic driver for fatigue crack nucleation? *Int. J. Plast.* 101, 213–229.

<https://doi.org/10.1016/j.ijplas.2017.11.005>

- Das, S., Armstrong, D.E.J., Zayachuk, Y., Liu, W., Xu, R., Hofmann, F., 2018a. The effect of helium implantation on the deformation behaviour of tungsten: X-ray micro-diffraction and nanoindentation. *Scr. Mater.* 146, 335–339.
<https://doi.org/10.1016/j.scriptamat.2017.12.014>
- Das, S., Hofmann, F., Tarleton, E., 2018a. Consistent determination of geometrically necessary dislocation density from simulations and experiments. *Int. J. Plast.* 109, 18–42. <https://doi.org/10.1016/j.ijplas.2018.05.001>
- Das, S., Liu, W., Xu, R., Hofmann, F., 2018b. Helium-implantation-induced lattice strains and defects in tungsten probed by X-ray micro-diffraction. *Mater. Des.* 160, 1226–1237.
<https://doi.org/10.1016/j.matdes.2018.11.001>
- Das, S., Yu, H., Tarleton, E., Hofmann, F., 2019. Orientation-dependent indentation response of helium-implanted tungsten. *Appl. Phys. Lett.* 114, 221905.
<https://doi.org/10.1063/1.5097403>
- Das, S., Yu, H., Tarleton, E., Hofmann, F., 2018b. Hardening and Strain Localisation in Helium-Ion-Implanted Tungsten. *arXiv Prepr.* arXiv1901.00745.
- Davoudi, K.M., Vlassak, J.J., 2018. Dislocation evolution during plastic deformation: Equations vs. discrete dislocation dynamics study. *J. Appl. Phys.* 123.
<https://doi.org/10.1063/1.5013213>
- DeBroglie, I., Beck, C.E., Liu, W., Hofmann, F., 2015. Temperature Dependence of Helium-Implantation-Induced Lattice Swelling in Polycrystalline Tungsten: X-ray Micro-Diffraction and Eigenstrain Modelling. *Scr. Mater.* 107, 4.
- Dennett, C.A., So, K.P., Kushima, A., Buller, D.L., Hattar, K., Short, M.P., 2018. Detecting self-ion irradiation-induced void swelling in pure copper using transient grating spectroscopy. *Acta Mater.* 145, 496–503.
<https://doi.org/https://doi.org/10.1016/j.actamat.2017.12.007>
- Derlet, P.M., Nguyen-Manh, D., Dudarev, S.L., 2007. Multiscale modeling of crowdion and vacancy defects in body-centered-cubic transition metals. *Phys. Rev. B - Condens. Matter Mater. Phys.* 76. <https://doi.org/10.1103/PhysRevB.76.054107>
- Duncan, R.A., Hofmann, F., Vega-Flick, A., Eliason, J.K., Maznev, A.A., Every, A.G., Nelson, K.A., 2016. Increase in elastic anisotropy of single crystal tungsten upon He-ion implantation measured with laser-generated surface acoustic waves. *Appl. Phys. Lett.* 109. <https://doi.org/10.1063/1.4964709>
- Dunne, F.P.E., Rugg, D., Walker, A., 2007. Lengthscale-dependent, elastically anisotropic, physically-based hcp crystal plasticity: Application to cold-dwell fatigue in Ti alloys. *Int. J. Plast.* 23, 1061–1083. <https://doi.org/10.1016/j.ijplas.2006.10.013>
- Dutta, B.N., Dayal, B., 1963. Lattice Constants and Thermal Expansion of Palladium and Tungsten up to 878 C by X-Ray Method. *Phys. status solidi* 3, 2253–2259.
<https://doi.org/10.1002/pssb.19630031207>
- Entler, S., Horacek, J., Dlouhy, T., Dostal, V., 2018. Approximation of the economy of fusion

- energy. *Energy* 152, 489–497. <https://doi.org/10.1016/j.energy.2018.03.130>
- Erinosho, T.O., Dunne, F.P.E., 2015. Strain localization and failure in irradiated zircaloy with crystal plasticity. *Int. J. Plast.* 71, 170–194. <https://doi.org/10.1016/j.ijplas.2015.05.008>
- Fang, X., Kreter, A., Rasinski, M., Kirchlechner, C., Brinckmann, S., Linsmeier, C., Dehm, G., 2018. Hydrogen embrittlement of tungsten induced by deuterium plasma: Insights from nanoindentation tests. *J. Mater. Res.* 33, 3530–3536. <https://doi.org/10.1557/jmr.2018.305>
- Featherston, F.H., Neighbours, J.R., 1963. Elastic constants of tantalum, tungsten, and molybdenum. *Phys. Rev.* 130, 1324–1333. <https://doi.org/10.1103/PhysRev.130.1324>
- Fleck, N.A., Hutchinson, J. w., 1997. Strain Gradient Plasticity. *Adv. Appl. Mech.* [https://doi.org/10.1016/S0065-2156\(08\)70388-0](https://doi.org/10.1016/S0065-2156(08)70388-0)
- Fukuda, M., Nogami, S., Hasegawa, A., Yabuuchi, K., 2015. Thermo-mechanical analysis of tungsten and its alloys monoblock divertor under heat load conditions relevant to a fusion reactor K-doped W 11, 99–103.
- Gibson, J., Armstrong, D., Roberts, S., 2014. The micro-mechanical properties of ion irradiated tungsten. *Phys. Scr.* T159. <https://doi.org/10.1088/0031-8949/2014/T159/014056>
- Gibson, J.S.K.-L., Roberts, S.G., Armstrong, D.E.J., 2015. High temperature indentation of helium-implanted tungsten. *Mater. Sci. Eng. A* 625, 380–384. <https://doi.org/10.1016/j.msea.2014.12.034>
- Guan, Y., Chen, B., Zou, J., Britton, T. Ben, Jiang, J., Dunne, F.P.E., 2017. Crystal plasticity modelling and HR-DIC measurement of slip activation and strain localization in single and oligo-crystal Ni alloys under fatigue. *Int. J. Plast.* 88, 70–88. <https://doi.org/10.1016/j.ijplas.2016.10.001>
- Hardie, C.D., Roberts, S.G., Bushby, A.J., 2015. Understanding the effects of ion irradiation using nanoindentation techniques. *J. Nucl. Mater.* 462, 391–401. <https://doi.org/https://doi.org/10.1016/j.jnucmat.2014.11.066>
- Heintze, C., Bergner, F., Hernández-Mayoral, M., 2011. Ion-irradiation-induced damage in Fe–Cr alloys characterized by nanoindentation. *J. Nucl. Mater.* 417, 980–983. <https://doi.org/https://doi.org/10.1016/j.jnucmat.2010.12.196>
- Heintze, C., Recknagel, C., Bergner, F., Hernández-Mayoral, M., Kolitsch, A., 2009. Ion-irradiation-induced damage of steels characterized by means of nanoindentation. *Nucl. Instruments Methods Phys. Res. Sect. B Beam Interact. with Mater. Atoms* 267, 1505–1508. <https://doi.org/https://doi.org/10.1016/j.nimb.2009.01.122>
- Hofmann, F., Mason, D.R., Eliason, J.K., Maznev, A.A., Nelson, K.A., Dudarev, S.L., 2015a. Non-Contact Measurement of Thermal Diffusivity in Ion-Implanted Nuclear Materials. *Sci. Rep.* 5, 16042. <https://doi.org/10.1038/srep16042>
- Hofmann, F., Nguyen-Manh, D., Gilbert, M.R., Beck, C.E., Eliason, J.K., Maznev, A.A., Liu, W., Armstrong, D.E.J., Nelson, K.A., Dudarev, S.L., 2015b. Lattice swelling and modulus change in a helium-implanted tungsten alloy: X-ray micro-diffraction, surface acoustic

- wave measurements, and multiscale modelling. *Acta Mater.* 89, 352–363.
<https://doi.org/10.1016/j.actamat.2015.01.055>
- Hosemann, P., Kiener, D., Wang, Y., Maloy, S.A., 2012. Issues to consider using nano indentation on shallow ion beam irradiated materials. *J. Nucl. Mater.* 425, 136–139.
<https://doi.org/https://doi.org/10.1016/j.jnucmat.2011.11.070>
- Hosemann, P., Maloy, S.A., Greco, R.R., Swadener, J.G., Romero, T., 2009. Oxygen effects on irradiated tantalum alloys. *J. Nucl. Mater.* 384, 25–29.
<https://doi.org/https://doi.org/10.1016/j.jnucmat.2008.09.027>
- Jiang, J., Britton, T.B., Wilkinson, A.J., 2013. Measurement of geometrically necessary dislocation density with high resolution electron backscatter diffraction: Effects of detector binning and step size. *Ultramicroscopy* 125, 1–9.
<https://doi.org/https://doi.org/10.1016/j.ultramic.2012.11.003>
- Jiang, J., Britton, T. Ben, Wilkinson, A.J., 2015. The orientation and strain dependence of dislocation structure evolution in monotonically deformed polycrystalline copper. *Int. J. Plast.* 69, 102–117. <https://doi.org/10.1016/j.ijplas.2015.02.005>
- Jiang, J., Yang, J., Zhang, T., Zou, J., Wang, Y., Dunne, F.P.E., Britton, T.B., 2016. Microstructurally sensitive crack nucleation around inclusions in powder metallurgy nickel-based superalloys. *Acta Mater.* 117, 333–344.
<https://doi.org/10.1016/j.actamat.2016.07.023>
- Klein, C.A., Cardinale, G.F., 1993. Young's modulus and Poisson's ratio of CVD diamond. *Diam. Relat. Mater.* 2, 918–923. [https://doi.org/10.1016/0925-9635\(93\)90250-6](https://doi.org/10.1016/0925-9635(93)90250-6)
- Knaster, J., Moeslang, A., Muroga, T., 2016. Materials research for fusion. *Nat. Phys.*
<https://doi.org/10.1038/NPHYS3735>
- Korsunsky, A.M., Dini, D., Dunne, F.P.E., Walsh, M.J., 2007. Comparative assessment of dissipated energy and other fatigue criteria. *Int. J. Fatigue* 29, 1990–1995.
<https://doi.org/https://doi.org/10.1016/j.ijfatigue.2007.01.007>
- Li, C., Zhu, D., Li, X., Wang, B., Chen, J., 2017. Thermal–stress analysis on the crack formation of tungsten during fusion relevant transient heat loads. *Nucl. Mater. Energy* 13, 68–73.
<https://doi.org/10.1016/j.nme.2017.06.008>
- Li, D., Zbib, H., Sun, X., Khaleel, M., 2014. Predicting plastic flow and irradiation hardening of iron single crystal with mechanism-based continuum dislocation dynamics. *Int. J. Plast.* 52, 3–17. <https://doi.org/https://doi.org/10.1016/j.ijplas.2013.01.015>
- Li, M., Morris, D.J., Jennerjohn, S.L., Bahr, D.F., Levine, L., 2009. Finite element analysis and experimental investigation of the Hertzian assumption on the characterization of initial plastic yield. *J. Mater. Res.* 24, 1059–1068. <https://doi.org/10.1557/jmr.2009.0134>
- Li, N., Fu, E.G., Wang, H., Carter, J.J., Shao, L., Maloy, S.A., Misra, A., Zhang, X., 2009. He ion irradiation damage in Fe/W nanolayer films. *J. Nucl. Mater.* 389, 233–238.
<https://doi.org/https://doi.org/10.1016/j.jnucmat.2009.02.007>
- Ma, L., Levine, L., Dixon, R., Smith, D., Bahr, D., 2012. Effect of the Spherical Indenter Tip Assumption on the Initial Plastic Yield Stress. *Nanoindentation Mater. Sci.* 22, 1656–

1661. <https://doi.org/10.5772/48106>

- Maisonnier, D., Cook, I., Pierre, S., Lorenzo, B., Edgar, B., Karin, B., Pace, D., Robin, F., Luciano, G., Stephan, H., Claudio, N., Prachai, N., Aldo, P., Neill, T., David, W., 2005. The European power plant conceptual study 79, 1173–1179. <https://doi.org/10.1016/j.fusengdes.2005.06.095>
- Marichal, C., Van Swygenhoven, H., Van Petegem, S., Borca, C., 2013. {110} Slip with {112} slip traces in bcc Tungsten. *Sci. Rep.* 3, 2547. <https://doi.org/10.1038/srep02547>
- Nye, J., 1953. Some geometrical relations in dislocated crystals. *Acta Metall.* 1, 153–162. [https://doi.org/10.1016/0001-6160\(53\)90054-6](https://doi.org/10.1016/0001-6160(53)90054-6)
- Ohashi, T., Kawamukai, M., Zbib, H., 2007. A multiscale approach for modeling scale-dependent yield stress in polycrystalline metals. *Int. J. Plast.* 23, 897–914. <https://doi.org/10.1016/j.ijplas.2006.10.002>
- Oliver, W.C., Pharr, G.M., 2004. Measurement of hardness and elastic modulus by instrumented indentation: Advances in understanding and refinements to methodology. *J. Mater. Res.* 19, 3–20. <https://doi.org/10.1557/jmr.2004.19.1.3>
- Pantleon, W., 2008. Resolving the geometrically necessary dislocation content by conventional electron backscattering diffraction. *Scr. Mater.* 58, 994–997. <https://doi.org/10.1016/j.scriptamat.2008.01.050>
- Reza, A., Yu, H., Mizohata, K., Hofmann, F., 2019. Thermal diffusivity degradation and point defect density in self-ion implanted tungsten. *arXiv Prepr. arXiv1909.13612*.
- Sauzay, M., Bavard, K., Karlsen, W., 2010. TEM observations and finite element modelling of channel deformation in pre-irradiated austenitic stainless steels - Interactions with free surfaces and grain boundaries. *J. Nucl. Mater.* 406, 152–165. <https://doi.org/10.1016/j.jnucmat.2010.01.027>
- Slabaugh, G.G., 1999. Computing Euler angles from a rotation matrix. <http://www.gregslabaugh.net/publications/euler.pdf> 6, 1–6.
- Srivastava, K., Gröger, R., Weygand, D., Gumbsch, P., 2013. Dislocation motion in tungsten: Atomistic input to discrete dislocation simulations. *Int. J. Plast.* 47, 126–142. <https://doi.org/10.1016/j.ijplas.2013.01.014>
- Stroh, A.N., 1957. A theory of the fracture of metals. *Adv. Phys.* 6, 418–465. <https://doi.org/10.1080/00018735700101406>
- Sweeney, C.A., Vorster, W., Leen, S.B., Sakurada, E., McHugh, P.E., Dunne, F.P.E., 2013. The role of elastic anisotropy, length scale and crystallographic slip in fatigue crack nucleation. *J. Mech. Phys. Solids* 61, 1224–1240. <https://doi.org/10.1016/j.jmps.2013.01.001>
- Taylor, G.I., 1934. The Mechanism of Plastic Deformation of Crystals. Part I. Comparison with Observations. *Proc. R. Soc. A Math. Phys. Eng. Sci.* 145, 388–404. <https://doi.org/10.1098/rspa.1934.0107>
- Tikkanen, P., Palonen, V., Jungner, H., Keinonen, J., 2004. AMS facility at the University of

- Helsinki. Nucl. Instruments Methods Phys. Res. Sect. B Beam Interact. with Mater. Atoms 223–224, 35–39. <https://doi.org/https://doi.org/10.1016/j.nimb.2004.04.011>
- Toloczko, M.B., Garner, F.A., Voyevodin, V.N., Bryk, V. V, Borodin, O. V, Mel'nychenko, V. V, Kalchenko, A.S., 2014. Ion-induced swelling of ODS ferritic alloy MA957 tubing to 500dpa. J. Nucl. Mater. 453, 323–333. <https://doi.org/https://doi.org/10.1016/j.jnucmat.2014.06.011>
- Villert, S., Maurice, C., Wyon, C., Fortunier, R., 2009. Accuracy assessment of elastic strain measurement by EBSD. J. Microsc. 233, 290–301. <https://doi.org/10.1111/j.1365-2818.2009.03120.x>
- Wan, V.V.C., Maclachlan, D.W., Dunne, F.P.E., 2014. A stored energy criterion for fatigue crack nucleation in polycrystals. Int. J. Fatigue 68, 90–102. <https://doi.org/10.1016/j.ijfatigue.2014.06.001>
- Wang, Y., Raabe, D., Klüber, C., Roters, F., 2004. Orientation dependence of nanoindentation pile-up patterns and of nanoindentation microtextures in copper single crystals. Acta Mater. 52, 2229–2238. <https://doi.org/10.1016/j.actamat.2004.01.016>
- Wei, N., Jia, T., Zhang, X., Liu, T., Zeng, Z., Yang, X., 2014. First-principles study of the phase stability and the mechanical properties of W-Ta and W-Re alloys. AIP Adv. 4, 57103. <https://doi.org/10.1063/1.4875024>
- Wilkinson, A.J., 1996. Measurement of elastic strains and small lattice rotations using electron back scatter diffraction. Ultramicroscopy 62, 237–247. [https://doi.org/10.1016/0304-3991\(95\)00152-2](https://doi.org/10.1016/0304-3991(95)00152-2)
- Wilkinson, A.J., Meaden, G., Dingley, D.J., 2006. High-resolution elastic strain measurement from electron backscatter diffraction patterns: New levels of sensitivity. Ultramicroscopy 106, 307–313. <https://doi.org/10.1016/j.ultramic.2005.10.001>
- Yao, Z., Hernández-Mayoral, M., Jenkins, M.L., Kirk, M.A., 2008. Heavy-ion irradiations of Fe and Fe–Cr model alloys Part 1: Damage evolution in thin-foils at lower doses. Philos. Mag. 88, 2851–2880. <https://doi.org/10.1080/14786430802380469>
- Yi, X., 2013. Electron Microscopy Study of Radiation Damage in Tungsten and Alloys.
- Yi, X., Jenkins, M.L., Briceno, M., Roberts, S.G., Zhou, Z., Kirk, M.A., 2013. *In situ* study of self-ion irradiation damage in W and W–5Re at 500 °C. Philos. Mag. 93, 1715–1738. <https://doi.org/10.1080/14786435.2012.754110>
- Yi, X., Jenkins, M.L., Kirk, M.A., Zhou, Z., Roberts, S.G., 2016. In-situ TEM studies of 150 keV W⁺ ion irradiated W and W-alloys: Damage production and microstructural evolution. Acta Mater. 112, 105–120. <https://doi.org/10.1016/j.actamat.2016.03.051>
- Zhu, C., Livescu, V., Harrington, T., Dipppo, O., Gray, G.T., Vecchio, K.S., 2017. Investigation of the shear response and geometrically necessary dislocation densities in shear localization in high-purity titanium. Int. J. Plast. 92, 148–163. <https://doi.org/https://doi.org/10.1016/j.ijplas.2017.03.009>
- Ziegler, J.F., Biersack, J., 2010. SRIM – The stopping and range of ions in matter (2010). Nucl.

Inst. Methods Phys. Res. B 268, 1818–1823.
<https://doi.org/10.1016/j.nimb.2010.02.091>

Zinkle, S.J., Was, G.S., 2013. Materials challenges in nuclear energy. *Acta Mater.* 61, 735–758. <https://doi.org/https://doi.org/10.1016/j.actamat.2012.11.004>